CBPF
Centro Brasileiro
de Pesquisas Físicas

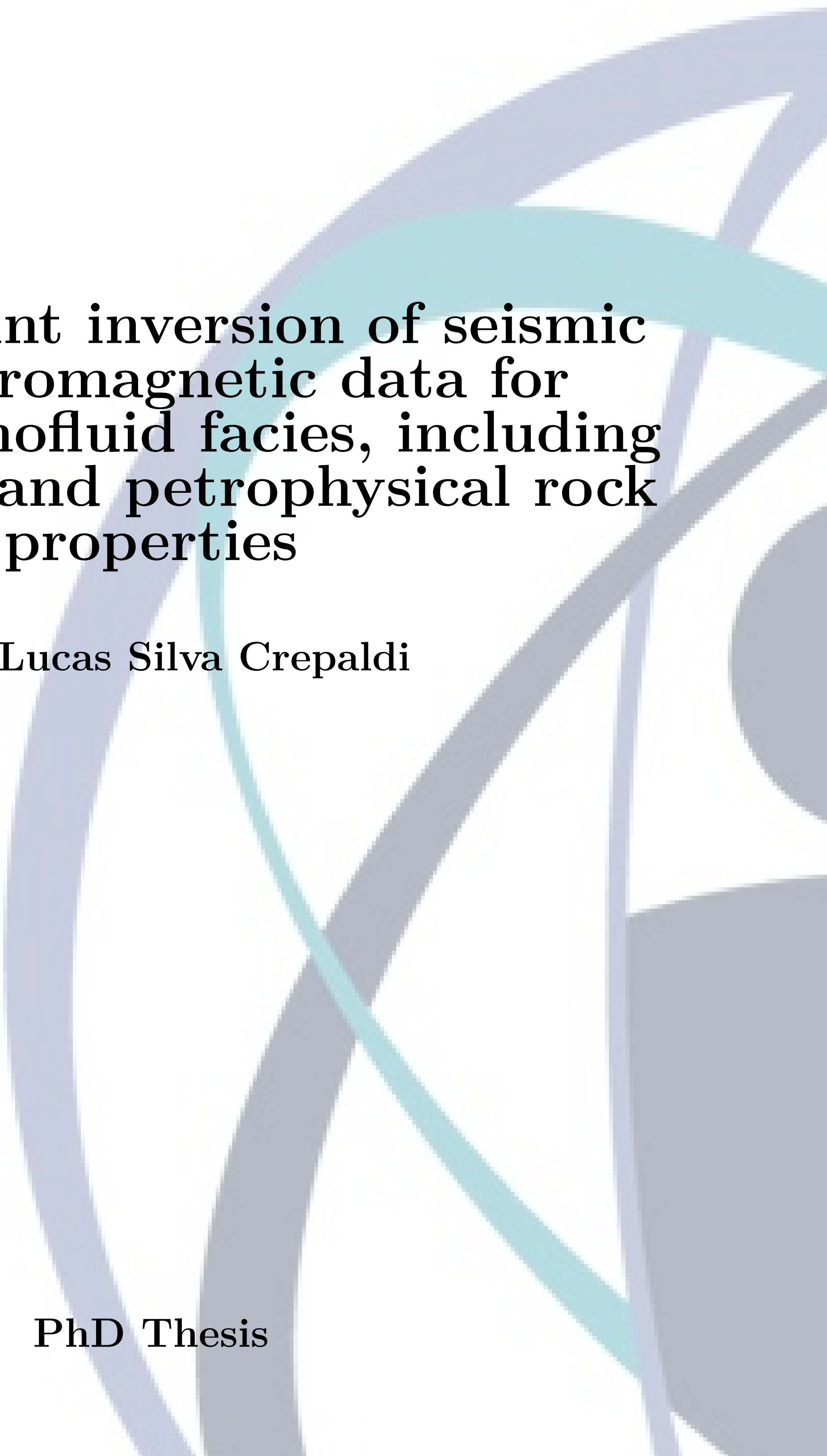

Bayesian joint inversion of seismic and electromagnetic data for reservoir lithofluid facies, including geophysical and petrophysical rock properties

João Lucas Silva Crepaldi

PhD Thesis

João Lucas Silva Crepaldi

Bayesian joint inversion of seismic and electromagnetic data for reservoir lithofluid facies, including geophysical and petrophysical rock properties

The thesis presented as part of the conditions to obtain the title of PhD in Physics from the Brazilian Center for Physics Research.

Supervisor: João Paulo Sinnecker
Co-supervisor: Ivan S. Oliveira

26 de julho de 2024

CBPF
Centro Brasileiro
de Pesquisas Físicas

MINISTÉRIO DA
CIÊNCIA, TECNOLOGIA
E INOVAÇÃO

GOVERNO FEDERAL
BRASIL
UNIÃO E RECONSTRUÇÃO

"BAYESIAN JOINT INVERSION OF SEISMIC AND ELECTROMAGNETIC DATA FOR RESERVOIR LITHO-FLUID FACIES INCLUGING GEOPHYSICAL AND PETROPHYSICAL ROCK PROPERTIES"

JOÃO LUCAS SILVA CREPALDI

Tese de Doutorado em Física apresentada no Centro Brasileiro de Pesquisas Físicas do Ministério da Ciência Tecnologia e Inovação. Fazendo parte da banca examinadora os seguintes professores:

João Paulo Sinnecker - Orientador/CBPF

Ivan dos Santos Oliveira Junior - Coorientador/CBPF

Ana Paula Oliveira Muller – PETROBRAS

Leonardo Azevedo – IST LISBOA

Luca Moriconi
Luca Roberto Augusto Moriconi – UFRJ

Luiz Alberto Santos – PETROBRAS

Rio de Janeiro, 12 de março de 2024.

*This work is dedicated to all those who raised,
accompanied, inspired, and taught me this far.*

Acknowledgements

We wish to thank Leonardo Alvim for the borehole data and his expertise in reservoir geophysics, Andrea Damasceno for borehole data, Bruno Rodrigues for suggestions and well-logs, Evaldo Mundim for suggestions, Erick Talarico for the discussion about facies inversion, Maury Correia for the insights and Avelino Crepaldi for reviewing and making suggestions regarding this text.

Those who search for the unattainable can still achieve the fullness of life if assuming that searching is the fundamental objective.

Resumo

Na exploração de petróleo, enquanto o método sísmico é sensível às litologias em reservatório, o eletromagnético é sensível à saturação de fluido. Um estudo de sensiblilidade valida essa complementaridade com resoluções parecidas. Uma abordagem Bayesiana é então proposta para estimar fácies de lito-fluido e outras propriedades de reservatório condicionadas a dados sísmicos e eletromagnéticos. As distribuições a priori são consideradas modos Gaussianos de propriedades geofísicas de rochas adquiridas diretamente ou convertidas de propriedades petrofísicas por modelagem calibrada de física de rochas. Uma generalização original inclui as duas distribuições na mesma integral de marginalização, que é resolvida analiticamente de modo a fornecer a probabilidade de um dado modelo de fácies condicionada aos dados geofísicos. Calcular essa probabilidade para todas as configurações de fácies possíveis pode ser impraticável, logo, um algoritmo Monte Carlo por Cadeia de Markov amostra modelos de maneira eficiente, fornecendo uma distribuição posteriori completa. A inversão utiliza dados geofísicos simulados de um modelo sintético 1D baseado no cenário geológico e um poço de um campo de petóleo marinho selecionado. Dois outros poços do mesmo reservatório foram utilizados para fornecer as distribuições a priori. Dados de poços, calibração da modelagem física das rochas e correspondência de fácies entre as distribuições a priori e o modelo sintético são apresentados e discutidos. Testes numéricos validam adaptações de modelagem direta não lineares na abordagem Gaussiana linearizada. Os dados geofísicos simulados autônomos e conjuntos são então invertidos para modelos de fácies lito-fluido sob diferentes condições a priori. Também foram testados dois cenários geoelétricos desafiadores, um com contrastes de resistividade mais baixos e outro com um modelo de fundo equivocado. Todos os resultados demonstram ganho em precisão e acurácia ao associar ambos os sinais geofísicos para se estimar a coluna de óleo. A abordagem Gaussiana linearizada permite o cálculo das propriedades geofísicas e petrofísicas das rochas através de inversões determinísticas locais sobre os diversos modelos de fácies amostrados. Tais inversões também demonstraram potencial para interpretações quantitativas de reservatórios.

Palavras-chave: Inversão Conjunta, Geophysica de Reservatório, Sísmica, CSEM, Bayes, Facies, Petrofísica.

Abstract

In the oil industry, whereas the seismic method is sensitive to reservoir lithologies, the electromagnetic is sensitive to fluid saturation. A sensitivity study supports this complementarity with similar resolutions. Hence, we propose a Bayesian approach to estimate lithofluid facies and other properties of reservoirs conditioned on seismic and electromagnetic data characterization. Prior distributions are assumed to be facies-related Gaussian modes of geophysical rock properties directly acquired or converted from petrophysical properties by calibrated rock-physics modeling. An original generalization includes these distributions in the same marginalization integral, analytically solved under a linearized Gaussian assumption to provide a facies model likelihood conditioned on geophysical data. Since computing this probability for all possible facies configurations may be impractical, a Markov Chain Monte Carlo algorithm efficiently samples models to provide a full posterior distribution. The inversion uses simulated geophysical data from a 1D synthetic model based on the geological scenario and a well from a selected marine oil field. Two other wells from the same reservoir were used to gather prior distributions. Data from the well, calibration of the rock-physics modeling, and facies matching between the priors and the synthetic model are presented and discussed. Numerical tests validate nonlinear forward modeling adaptations on the assumed linearized Gaussian approach. The simulated stand-alone and joint geophysical datasets are then inverted for lithofluid facies models under different prior inputs. Two challenging geoelectric scenarios were also tested, one with lower resistivity contrasts and another with a misguided background model. All results demonstrate a gain in precision and accuracy when associating both geophysical signals to estimate the oil column. The linearized Gaussian approach allows the computation of the conditional distributions of geophysical and petrophysical rock properties by applying local deterministic inversions over the many sampled facies models. The linearized Gaussian approach allows the computation of the conditional distributions of geophysical and petrophysical rock properties by applying local deterministic inversions over the many sampled facies models. Such application also shows potential for quantitative reservoir interpretations.

Keywords: Joint Inversion, Reservoir Geophysics, Seismic, CSEM, Bayes, Facies, Petrophysics.

Contents

Resumo **9**

Abstract **11**

1 INTRODUCTION **25**

2 GEOPHYSICAL AND ROCK-PHYSICS MODELING **29**
2.1 Seismic modeling **29**
2.2 Geoelectric model **29**
2.3 Electromagnetic modeling **30**
2.4 Rock-physics modeling **32**

3 SENSITIVITY ANALYSIS (MOTIVATION) **35**
3.1 Synthetic model **35**
3.2 Geometrical constraint **36**
3.3 Petrophysical constraints **38**
3.4 Geometrical and petrophysical constraints **39**
3.5 Partial conclusion **40**

4 METHODOLOGY **43**
4.1 Theory **43**
4.1.1 Bayesian inferences 43
4.1.2 Proposed generalization 44
4.1.3 Solving the integrals 45
4.2 Implementation **48**
4.2.1 Facies from geophysical data 48
4.2.2 Local inversions 49

5 DATA ANALYSIS **53**
5.1 Well data **53**
5.2 Rock-physics calibration **57**
5.3 Facies from priors **58**
5.4 Geophysical linearization **60**

6 APPLICATIONS AND DISCUSSIONS **63**
6.1 Inversion for facies **63**
6.2 Lower resistivity contrast **65**

6.3 Misguided overburden 65
6.4 Inversions for rock properties 68

7 CONCLUSION AND PERSPECTIVES 73

APPENDIX 75

APPENDIX A – PETROELASTICAL MODEL 77

APPENDIX B – JACOBIAN OF PETROELASTICAL MODEL . . 81

BIBLIOGRAPHY 89

List of Figures

Figure 1 – Representation of marine seismic acquisition. A vessel tows the air gun source and hydrophones stream close to the water surface. The red rays depict the seismic wave paths. 30

Figure 2 – A numerical example of AVA seismic modeling: the 12 reflection coefficients are a function of the incident angle, and the 13 layers elastic model in time domain 4 ms-discretized as the seismic signal sampling. These reflectivity series are convolved with the respective wavelets, taking the 12 central samples as the modeled seismic signal. The peak of the wavelets normalizes the amplitudes. 31

Figure 3 – The left frame is the resistivity model, including the background, representative oil, and brine sand layers inside the 70.2 m-IOI. The other frames are color maps of percent anomaly for $|E_x|$ response on the presence of a 70 Ωm-5.4 m layer on the top of IOI, compared to the response to 1 Ωm homogeneous IOI, for inline and broadside source-receiver geometries, over frequency versus offset axes. Black lines are the noise threshold of $10^{-15.5}$ V/Am^2. Red dots are the chosen offset limit and frequency. 32

Figure 4 – Scheme of marine CSEM acquisition. A vessel tows the alternated current horizontal bipole tens of meters above the sea floor. At the same time, electromagnetic receivers deployed on the ocean bottom record the transmitted signal that carries influences of the whole medium, including the subsurface. (Courtesy of Scripps Institute of Oceanography). 33

Figure 5 – The inline and broadside source-receiver arrangement employed in this work. 33

Figure 6 – Above, the CSEM inline and broadside electric fields at the chosen frequency and offsets, for homogeneous and anomalous IOI. Below are the corresponding ratios between the anomalous and homogeneous IOI responses. 34

Figure 7 – Synthetic 1D model of a reservoir, z is depth relative to the top of the IOI, smooth gray lines are the 5.4 m discretization, and colors indicate the lithofluid facies. 36

Figure 8 – Three maps of the misfit function varying the velocity Vp and thickness h of the oil column. At left for seismic stand-alone, at the center for CSEM with fixed *Res*, and right for the arithmetic average of the previous ones. The symbol * marks the reference values. 37

Figure 9 – Three maps of the misfit function varying the resistivity and thickness h of the oil column. At left for CSEM stand-alone, at the center for seismic with fixed Vp, and right for the arithmetic average of the previous ones. The symbol * marks the reference values. 37

Figure 10 – Three maps of the misfit function varying the oil column's porosity Φ and water saturation Sw. At left for seismic stand-alone, at the center for CSEM stand-alone, and right for the arithmetic average of the previous ones. The symbol * marks the reference values. 38

Figure 11 – Three maps of the misfit function varying the oil column's porosity Φ and water saturation Sw. At left for seismic stand-alone, at the center for CSEM stand-alone, and right for the arithmetic average of the previous ones. The data weight and added noise include the calibration misfit. The symbol * marks the reference values. 39

Figure 12 – Three maps of the misfit function varying the thickness h and water saturation Sw of the oil column. At left for the seismic stand-alone, at the center for the CSEM stand-alone, and right for the arithmetic average of the previous ones. The symbol * marks the reference values. 39

Figure 13 – Three maps of the misfit function varying the thickness h and water saturation Sw of the oil column. At left for the seismic stand-alone, at the center for the CSEM stand-alone, and right for the arithmetic average of the previous ones. The data weight and added noise include the calibration misfit. The symbol * marks the reference values. 40

Figure 14 – Color map of covariance matrices Cm and $TCrT^T$, for three layers model. Including the three chosen lithofluid facies (shale, brine sand, and oil sand), indicated on layers, and the four geophysical properties marked on elements of Cm picture (seismic velocities Vp and Vs, density Dens, and resistivity Res); and similar to $TCrT^T$ picture. 47

Figure 15 – Block diagram for the facies inversion algorithm. Facies discriminate the rock properties from well-logs, and the electrical anisotropy ratio θ rescales the resistivities, calibrating rock-physics parameters to provide the misfit, means, and Jacobian for the geophysical transformed properties. The inputs are the means and covariances extracted from these treated prior well data, seismic and CSEM data, prior weight α, and the initial model. Seismic and CSEM modeling and Jacobians are the primary external functions of the looping. Aleatory widowing and facies sampling are subroutines with fixed parameters. The acceptance condition is based on MCMC. The accepted sample is inputted to build new facies proposal and stored to update the posterior distribution. . . 50

Figure 16 – The lithological columns of prior wells (WP1) and (WP2), test well (WT) in depth. The lithofacies are indicated in textures without discriminating fluid saturation. The horizontal thickest lines indicate the top and bottom of the interval of interest (IOI) and oil-water contact (OWC) at each well. 54

Figure 17 – The first two columns are the original and upscaled lithofluid facies of the WT in depth. The following frames are the rock properties profiles, with the original WT profiles in black, transformed vertical resistivity in green, and the synthetic model in magenta. Prior averages in blue lines for WP1, red lines for WP2, and dashed lines are their respective intervals of one standard deviation. 55

Figure 18 – Crossplots of shale volume Vsh versus porosity Φ, elastic Is versus acoustic Ip impedances, and vertical resistivity $\mathrm{Res_v}$ versus water saturation Sw. The contours correspond to one standard deviation for each pair of properties distribution related to facies, prior WPs, and reference WT wells. In legend, Ptr means that the corresponding geophysical property is transformed from petrophysical modeling. 56

Figure 19 – Calibrated rock-physics parameters for each of the three employed facies and WP1 and WP2. Petroelastic parameters: the K and μ refer to bulk and shear moduli respectively, ρ to density, Res to resistivity, g to grain, sh to shale, w to water, hc to hydrocarbon, C to coordination number, Φ_0 to critical porosity. Petroelectric parameters: a is tortuosity, m and n are cementation and saturation exponents for grain and shale in the rock matrix. 57

Figure 20 – Color map of 13-layer (y-axis) facies models inferred by applying the WP1 and WP2 priors over the synthetic model of geophysical rock properties. Frames for elastic-only (Elastic), resistivity-only (Electric), and (Joint) rock properties present a sequence of 11 inferred facies models related to α values regularly spaced between $0 \leq \alpha \leq 1$ (x-axis). Black lines are the reference facies transitions. 59

Figure 21 – Comparison between linear and nonlinear geophysical responses for the synthetic model: a) The three angle-related frames contain the seismic signals as indicated in the legend. b) The upper frames contain the CSEM inline and broadside signals; the clear nonlinear signal normalizes the others on the lower frames. 61

Figure 22 – Histograms of acceptance rate for 100 simulations per experiment based on a sequence of increasing oil column models for seismic and CSEM stand-alone and joint data. The blue bars are nonlinear, and the red bars are linear modeling, each covering a 0.1 acceptance rate interval. On the models, gray is shale, yellow is brine sand, green is oil sand, and black lines are the reference facies transitions. 62

Figure 23 – Color map of 13-layer (y-axis) MAP facies models inverted geophysical synthetic data. Frames for seismic-only (SS), CSEM-only (EM), and joint inversions (SEM) present a sequence of 11 facies models related to α values regularly spaced between $0 \leq \alpha \leq 1$ (x-axis). Each inversion realization is applied to data with different noise seeds. Gray is shale, yellow is brine sand, green is oil sand, and black lines are the reference facies transitions. 64

Figure 24 – Color map of 13-layer (y-axis) MAP facies models inverted from geophysical simulated data over the less resistive synthetic model Res_h. Frames for seismic-only (SS), CSEM-only (EM), and joint inversions (SEM) present a sequence of 11 facies models related to α values regularly spaced between $0 \leq \alpha \leq 1$ (x-axis). Each inversion realization is applied to data with different noise seeds. Gray is shale, yellow is brine sand, green is oil sand, and black lines are the reference facies transitions. . . 66

Figure 25 – Color map of 13 by 13 elements of the ratio between sensitivity matrices $(G_c^T G_c)/(G_r^T G_r)$, where G_c and G_r are the Jacobians of the more conductive more resistive models respectively. 67

Figure 26 – Color map of 13-layer (y-axis) MAP facies models inverted from geophysical simulated data with CSEM perturbed by a resistive layer on the overburden. Frames for seismic-only (SS), CSEM-only (EM), joint (SEM), and SEM with enhanced seismic inversions present a sequence of 11 facies models related to α values regularly spaced between $0 \leq \alpha \leq 1$ (x-axis). Each inversion realization is applied to data with different noise seeds. Gray is shale, yellow is brine sand, green is oil sand, and black lines are the reference facies transitions. 68

Figure 27 – Joint geophysical data inversion for facies, geophysical and petrophysical properties, with $\alpha = 0.5$ and priors from WP1. The first two columns are the facies iterations and MAP, and the black lines are the reference facies transitions. On the properties profiles, cyan lines are the MAP, color maps are the posterior probabilities, and black lines are the reference values. 69

Figure 28 – Joint geophysical data inversion for facies, geophysical and petrophysical properties, with $\alpha = 0.5$ and priors from WP2. The first two columns are the facies iterations and MAP, and the black lines are the reference facies transitions. On the properties profiles, cyan lines are the MAP, color maps are the posterior probabilities, and black lines are the reference values. 70
Figure 29 – Inversion for facies, geophysical and petrophysical properties, with $\alpha = 0.5$ and priors from WT. The first two columns are the facies iterations and MAP, and the black lines are the reference facies transitions. On the properties profiles, cyan lines are the MAP, color maps are the posterior probabilities, and black lines are the reference values. 71
Figure 30 – Misfit evolution for geophysical and petrophysical local inversions in the 2000 facies iterations of joint geophysical data inversion, for WP1 with $\alpha = 0.5$. 71
Figure 31 – Geophysical data and joint inversion responses: a) The frames separate seismic signals by the indicated angles with the contaminated data in black, the sample's responses in red, and the MAP response in cyan. b) The upper frames are CSEM inline and broadside electric contaminated data in magenta, the clear signal in black, the samples responses in red, and the MAP response in cyan; the lower frame is the same data normalized by the clear signal. c) The same as (b) for CSEM broadside signal. 72

List of Tables

Table 1 – Table of synthetic model properties by lithofluid facies: V_p and V_s are compression and shear velocities respectively, ρ is density. Φ is porosity, S_w is water saturation and V_{sh} is shale volume (dimensionless values). . 35

List of abbreviations and acronyms

AVA	Amplitude Versus Angle
AVO	Amplitude Versus Offset
CSEM	Controlled-Source Electromagnetic
CMP	Common Mid Point
MCMC	Markov Chain Monte Carlo
PDF	Probability Density Function
ND	Normal Distribution
MAP	Maximum a Posteriori Probability
IOI	Interval of Interest
OWC	Oil-Water Contact
WP	Prior Well
WT	Test Well
SS	Seismic Stand-Alone
EM	CSEM Stand-Alone
SEM	Seismic plus CSEM

1 Introduction

The goal of mitigating risk in hydrocarbon exploration and reservoir recovery has driven the development of tools to integrate seismic data, well-logs, core samples, and geologic models in reservoir characterization [1]. There are various approaches for quantitative estimation of reservoir properties from seismic inversion; some invert for elastic and petrophysical properties as continuous parameters [2], and others use facies estimation [3–7]. However, mapping fluid saturation from seismic signals faces critical limitations as the rock matrix dominates the elastic moduli and density of the bulk [8]. Such limitations make the interpretation highly dependent on prior knowledge [9], signal processing, and acquisition [10].

Conversely, the electrolytic conductivity of fluids in the connected pore spaces dominates the resistivity of sedimentary rocks [8]. Indeed, resistivity well-logs are the primary tool for indirectly measuring fluid saturation throughout a borehole. In particular, the observed strong contrasts in resistivity of a siliciclastic reservoir at the oil-brine interface have led to the increasing use of electromagnetic geophysical methods for mapping fluids in marine reservoirs [11–14].

Despite its relatively recent history, the marine Controlled-Source Electromagnetic (CSEM) method has been successfully applied to offshore hydrocarbon exploration [11, 14, 15], often at the intermediate stage of field development: after seismic interpretation, since CSEM acquisition is focused on leads and the interpretation of the acquired signals depends on prior information, and before reservoir characterization [11], due to the limited signal resolution compared to the typical geologic scale in which reservoir engineers are interested.

Some approaches invert the stand-alone CSEM data for a resistivity model that focuses on the seismically derived zone of interest and then use that resistivity and elastic rock properties from seismic inversion to estimate petrophysical properties such as porosity, saturation, shale volume, and lithofluid facies by calibrated rock-physics modeling [13, 14].

However, constraining resistivity models with seismically derived regularization and prior models may need to be revised or more accurate in recovering models at the inner reservoir scale. For instance, assigning transverse resistance for the interval from CSEM-only inversions does not contribute to the seismic mapping of the oil-water contact. It requires a circular interpretation process [16]. Therefore, the seismic resolution to lithology should be associated with CSEM sensitivity to fluid saturation by simultaneous joint inversion linked in the model domain [17].

Techniques of seismic and CSEM joint inversion have been proposed linking elastic to electrical models by spatial constraints [18], petrophysical coupling [19–22], and facies categorization [7, 23]. Inverting for facies links electric to elastic models by spatial discretization associated with facies-related prior means and covariances of geophysical rock properties. Petrophysical coupling can be explicitly introduced when using petrophysical parameters as prior distributions and associating rock-physics with geophysical modeling in the forward function [24] or, as in this work, implicitly when using petrophysical parameters transformed by rock-physics modeling to compose the prior distributions.

Over the last decade, several works have been concerned with facies inversion from geophysical data, often presenting the Bayesian approach as a natural framework to solve inverse problems that combine categorical and continuous variables. The posterior probability density function (PDF) defines the target solution for the model parameters, providing the maximum posterior probability (MAP) model and related uncertainty. Given the number of cells in 3D reservoir models [10], the full stochastic evaluation of the posterior PDF [23, 24] might be very costly when modeling CSEM and seismic signals by numerical solvers of differential or integral equations. [25–27]. In this thesis, we use 1D models and forward functions to concept-proof, although we are interested in developing an inversion routine prepared to efficiently incorporate 3D models and functions.

We propose a Bayesian joint inversion of seismic and CSEM data to estimate models of lithofluid facies, in contrast with [23], by using a linearized Gaussian approach where the marginalization over geophysical rock properties is found analytically [6, 28]. Although the Zoeppritz reflectivity [8, 29] and CSEM 1D modeling [30] are nonlinear functions, they are used as forward modeling and assumed to be linear approximations around the facies-related averages to take advantage of such analytical solutions. Numerical tests validate this adaptation of the linearized Gaussian approach for the given conditions.

The petrophysical prior distributions converted to geophysical rock properties by calibrated rock-physics modeling may introduce distinct facies-related means and covariances than directly acquired geophysical rock properties. Hence, we assemble prior distributions of geophysical and transformed petrophysical rock properties in the marginalization integrals. We also linearize the rock-physics modeling around the averages. A proposed parameter weights these distributions, providing stand-alone geophysical [6] or petrophysical priors at the edges and joint distributions [2, 5, 23, 31, 32] at the middle of its range.

The proposed linearizations using analytical Jacobians of forward functions efficiently evaluate the data-conditioned likelihood for a given facies model (posterior probability). However, there are F^N possible configurations for F facies arranged in N layers, and computing them may be impracticable. Thus, a Markov Chain Monte Carlo algorithm [33] samples models through that likelihood to provide a full posterior distribution in reasonable run time.

As in [6] and different than in [23], the model layer thickness is equivalent to the seismic data sampling, which means a model discretization on the limit of signal resolution. Unlike these works, we do not impose spatial correlation between layers in the covariance matrices to focus on evaluating the inversion accuracy for each given dataset. However, we set correlations between layers in the model perturbation.

A siliciclastic marine reservoir in the Campos Basin in Brazil [10] was selected to validate the methodology in a realistic scenario. We used two wells, one as prior information and another as a base for the synthetic model to simulate the geophysical data. After presenting and discussing the well's data, rock-physics calibration, and matching between priors and the synthetic model, we apply the proposed lithofluid facies inversion to the simulated data for many prior settings and compare stand-alone with joint inversions.

To challenge the CSEM inversions, we simulate two pessimistic scenarios, one with lower resistivity contrasts for the fluid saturation and another with a resistive layer in the overburden, which is ignored during forward modeling. We also test many datasets in these simulations.

The linearized Gaussian approach allows us to compute the conditional distributions of geophysical and petrophysical rock properties by sampling linear transformations over their respective means and covariances on each accepted facies model [4, 5, 32]. Instead, because we use nonlinear forward functions, nonlinear inversions [34, 35] are performed to minimize the residuals in these local inversions. Finally, our method is applied to joint geophysical data and joint prior distributions, providing profiles of posterior distributions for the rock properties in three inversion experiments, each using one of the three wells as a prior, including the testing well itself. We approach this feature as a supplementary subroutine without testing many parameterizations and detailing the results.

This Thesis is organized as follows: Chapter 2 presents seismic, CSEM, and rock-physics modeling. Chapter 3 is a sensitivity analysis of seismic and CSEM signals to a simplified reservoir model. Chapter 4 describes the linearized Gaussian methodology and computational implementation. Chapter 5 presents the borehole data, quality controls, and aspects of the proposed geophysical linearization. Finally, in Chapter 6, we apply the facies inversion to the synthetic model with many prior conditions and local inversions for rock properties. Chapter 7 is the conclusions and perspectives. Appendix A presents the mathematical formulation of the elastic rock-physics modeling, and Appendix B presents the Fréchet derivative of this composed formulation.

2 Geophysical and rock-physics modeling

The modeling functions and parameterizations used in this work are described as follows.

2.1 Seismic modeling

The seismic modeling is based on the Convolutional Model with Zoeppritz *Rpp* reflection component [8], simulating a conventional marine seismic acquisition (Figure 1, image extracted from [36]). The typical AVA attribute angles [20] of 20-degree, 30-degree, and 45-degree are chosen to cover the valid range of the Aki-Richards approximation [37] in the Jacobian calculation. These angles simulate the *near*, *mid*, far gathers of partially staked angles on the widely employed AVO attribute [38].

In that time-domain paradigm, the interval of interest (IOI) is a layered model of compression V_p, shear V_s velocities, and density ρ, discretized in $n = 13$ layers of 5.4 m thickness, corresponding to 4 ms two-way travel time for 2.7 km/s migration velocity. Then, the reflection coefficients are calculated and convolved with wavelets relative to each angle, with about 30 Hz peak frequency f_M [39] extracted from generic field data. The reflection coefficients must be convolved with the wavelets to honor the frequency content of the in-field data, and the $n-1$ central samples of the convolved vector are sufficient for the inversion (Figure 2) [6]. Gaussian noise is added with 10 % variance of the noise-free signal, simulating data noise and uncertainties on the wavelet estimation [4].

Instead of using the derivatives of the Zoeppritz coefficients, the Jacobian matrix of the seismic forward function is built with the Aki-Richards coefficient matrix A [37] multiplied by the differential operator D, convoluted with the wavelets $S * AD$ [4]. As the geophysical properties are logarithmically scaled to be inversion parameters, the Aki-Richards approximation is more computationally convenient and suitable for those angles, velocity contrasts, and noise level [37].

2.2 Geoelectric model

According to the geoelectric scenario of the selected reservoir, the 1D resistivity model as input is composed of the 70.2 m-IOI inserted below 0.3 Ωm-1.3 km sea water plus 1 Ωm-1.5 km overburden; above 1 Ωm-500 m followed by 4 Ωm-500 m underburden sediments; over a 100 Ωm half-space basement (Figure 3).

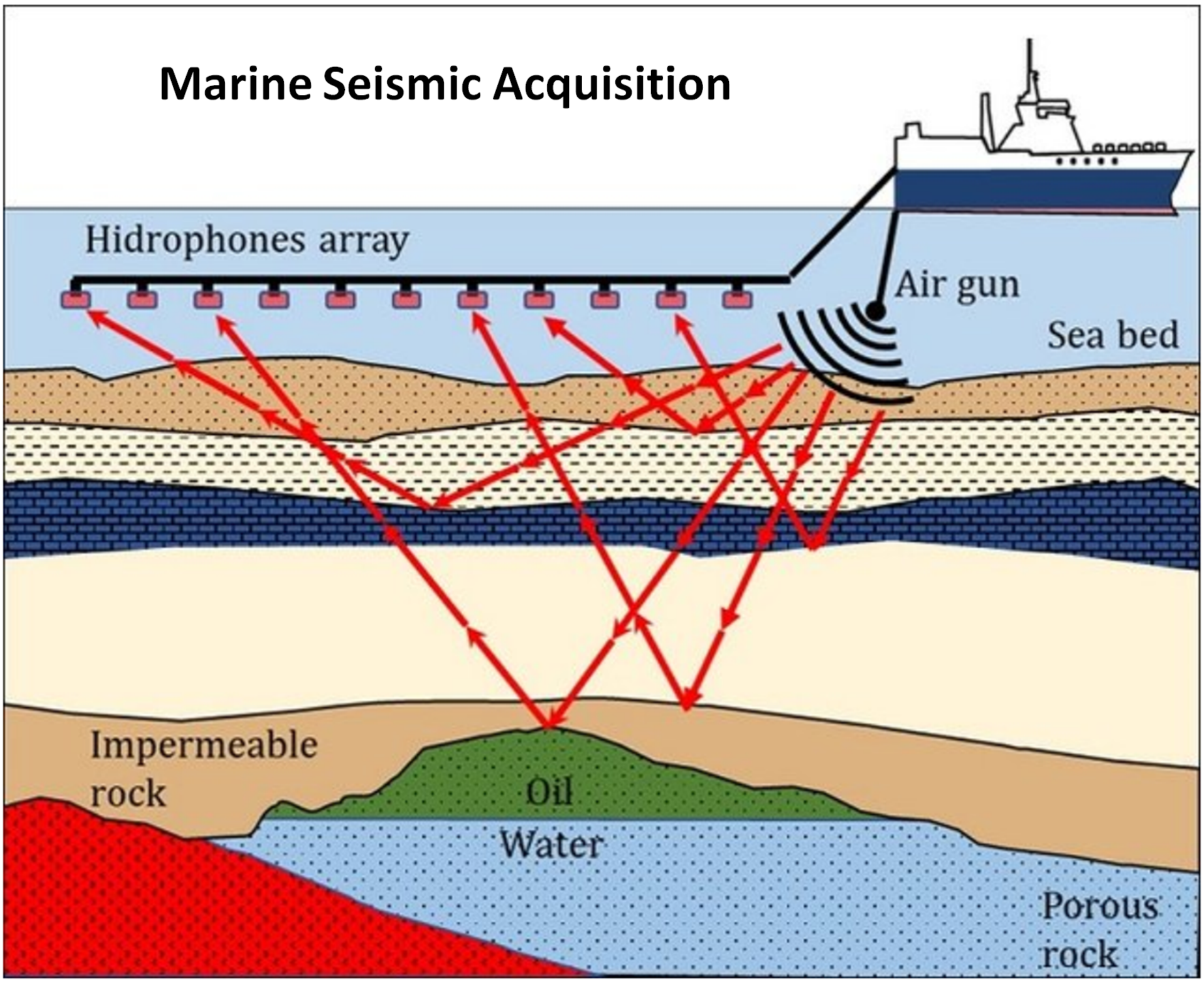

Figure 1 – Representation of marine seismic acquisition. A vessel tows the air gun source and hydrophones stream close to the water surface. The red rays depict the seismic wave paths.

2.3 Electromagnetic modeling

The algorithm described in [30] calculates the CSEM 1D responses on a receiver placed at the sea floor (see Figure 3) for a normalized horizontal electric dipole towed 50 m above the receiver depth [40, 41]. The Jacobian matrix for inversion also uses the analytical derivatives in [30].

Figure 3 shows the CSEM sensitivity to a 70 Ωm-5.4 m resistive layer, simulating one oil sand layer on the employed discretization, just above a 1 Ωm-64.8 m conductive layer, representing the other 12 layers of the IOI filled with brine sand. The color map presents the percent anomaly in the amplitude of this model's horizontal electric field $|E_x|$ responses, related to the corresponding responses for the entire IOI filled with a homogeneous 1 Ωm layer. The anomaly color maps are plotted over the offsets in the x-axis and the frequencies in the y-axis for inline and broadside source-receiver arrangements in each frame. The black lines indicate the employed $10^{-15.5}$ V/Am^2 noise threshold, a

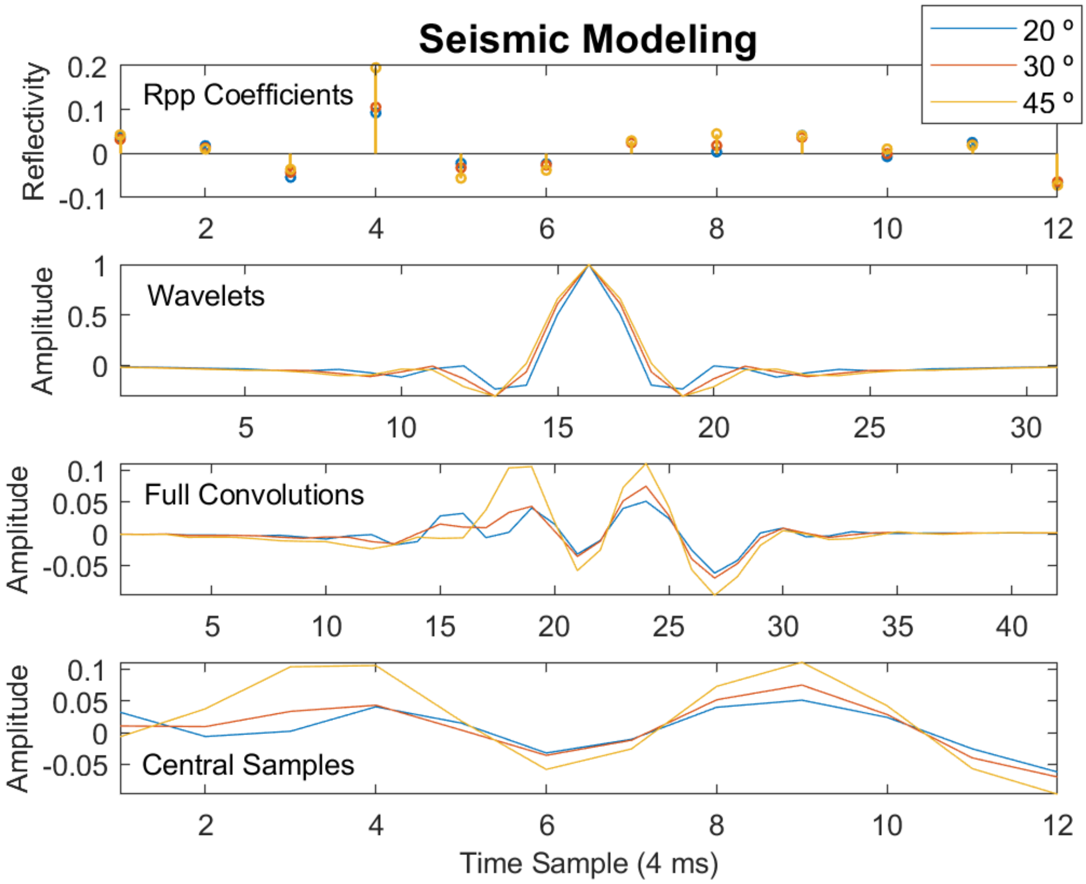

Figure 2 – A numerical example of AVA seismic modeling: the 12 reflection coefficients are a function of the incident angle, and the 13 layers elastic model in time domain 4 ms-discretized as the seismic signal sampling. These reflectivity series are convolved with the respective wavelets, taking the 12 central samples as the modeled seismic signal. The peak of the wavelets normalizes the amplitudes.

slightly higher value than in [11], as it is achievable in current surveys.

Figure 4 depicts the marine CSEM survey.

Figure 5 shows a map of the two source-receiver arrangements. Note that there is only one receiver since our modeling is 1D.

We chose 0.75 Hz frequency with a 2.1 to 6 km offset range according to a compromise between sensitivity to the resistive layer and the number of data points. Signals below 2 km offset have dispensable anomaly levels and are problematic in-field data, and 6 km is close to the noise threshold (red dots in Figure 3). We use a source position interval of 100 m as a conventional acquisition parameter.

Figure 6 shows the inline and broadside electric fields at 0.75 Hz in the chosen offset range, for homogeneous and anomalous IOI (Figure 3).

The electromagnetic data is contaminated with standard deviation noise at 3 to 5 % [23] of the signal, linearly increasing with the offset. The Gaussian noise distribution

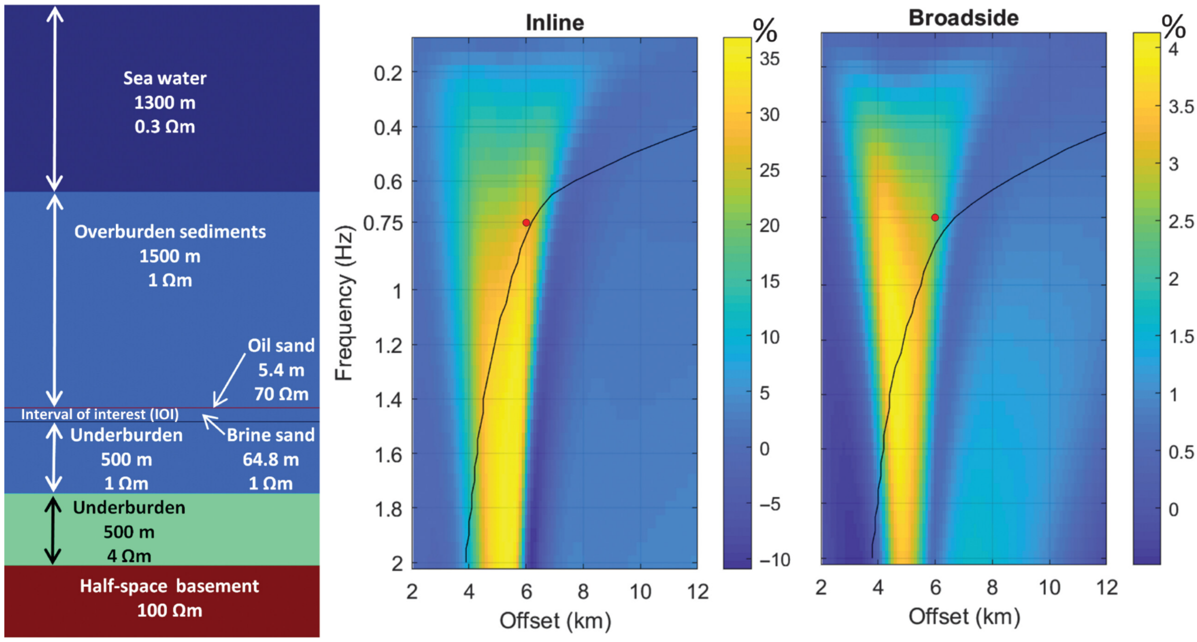

Figure 3 – The left frame is the resistivity model, including the background, representative oil, and brine sand layers inside the 70.2 m-IOI. The other frames are color maps of percent anomaly for $|E_x|$ response on the presence of a 70 Ωm-5.4 m layer on the top of IOI, compared to the response to 1 Ωm homogeneous IOI, for inline and broadside source-receiver geometries, over frequency versus offset axes. Black lines are the noise threshold of $10^{-15.5}$ V/Am^2. Red dots are the chosen offset limit and frequency.

is treated on a logarithmic scale to be consistent with the adopted data space.

Evaluating the inclusion of multi-frequency, multi-component, and phase showed little contribution compared to the increasing complexity of the responses analysis. Hence, as a matter of simplicity, inverting one frequency and only the amplitude of the horizontal inline and broadside electric fields are sufficient for the scope of this work [30, 42, 43].

2.4 Rock-physics modeling

Elastic rock-physics modeling is a granular model composed by coupling some sub-models. It starts from the Voigh-Reuss Average for bulk K_{mat} and shear G_{mat} moduli of the rock matrix, composed of grains and shale; Hertz-Mindlin Model introduces the effective pressure P_{eff}, coordination number C and critical porosity Φ_0; and Hashin-Shtrikman includes the porosity Φ, with a Stiff Sand Model for sandstone and a Soft Sand Model for shale stone.

The Gassman Model includes the water saturation S_w, and the Constitutive Equations give the compressional V_p and shear V_s velocities from the bulk modulus of the saturated rock K_{sat}, the shear modulus of porous media G_{dry} and the total density ρ [8].

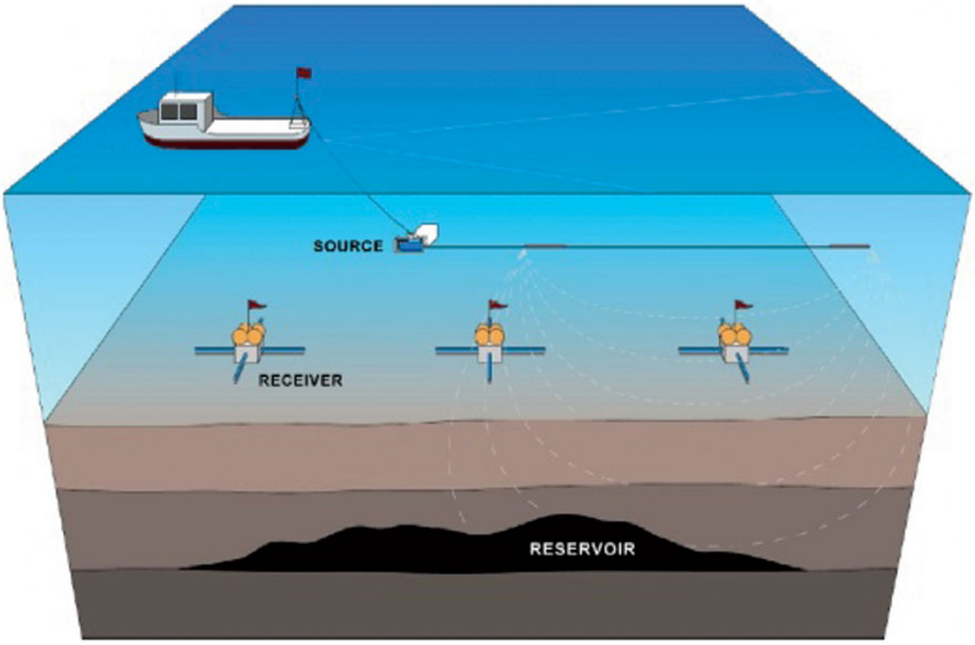
SOURCE
RECEIVER
RESERVOIR

Figure 4 – Scheme of marine CSEM acquisition. A vessel tows the alternated current horizontal bipole tens of meters above the sea floor. At the same time, electromagnetic receivers deployed on the ocean bottom record the transmitted signal that carries influences of the whole medium, including the subsurface. (Courtesy of Scripps Institute of Oceanography).

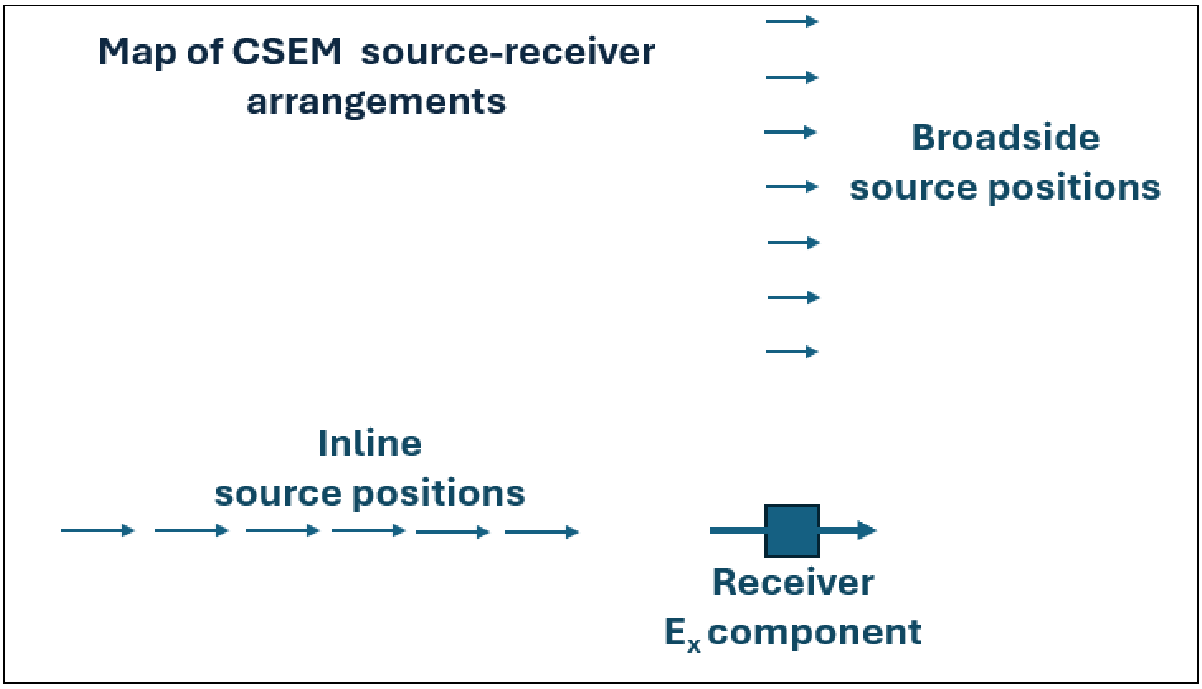
Map of CSEM source-receiver arrangements
Broadside source positions
Inline source positions
Receiver E_x component

Figure 5 – The inline and broadside source-receiver arrangement employed in this work.

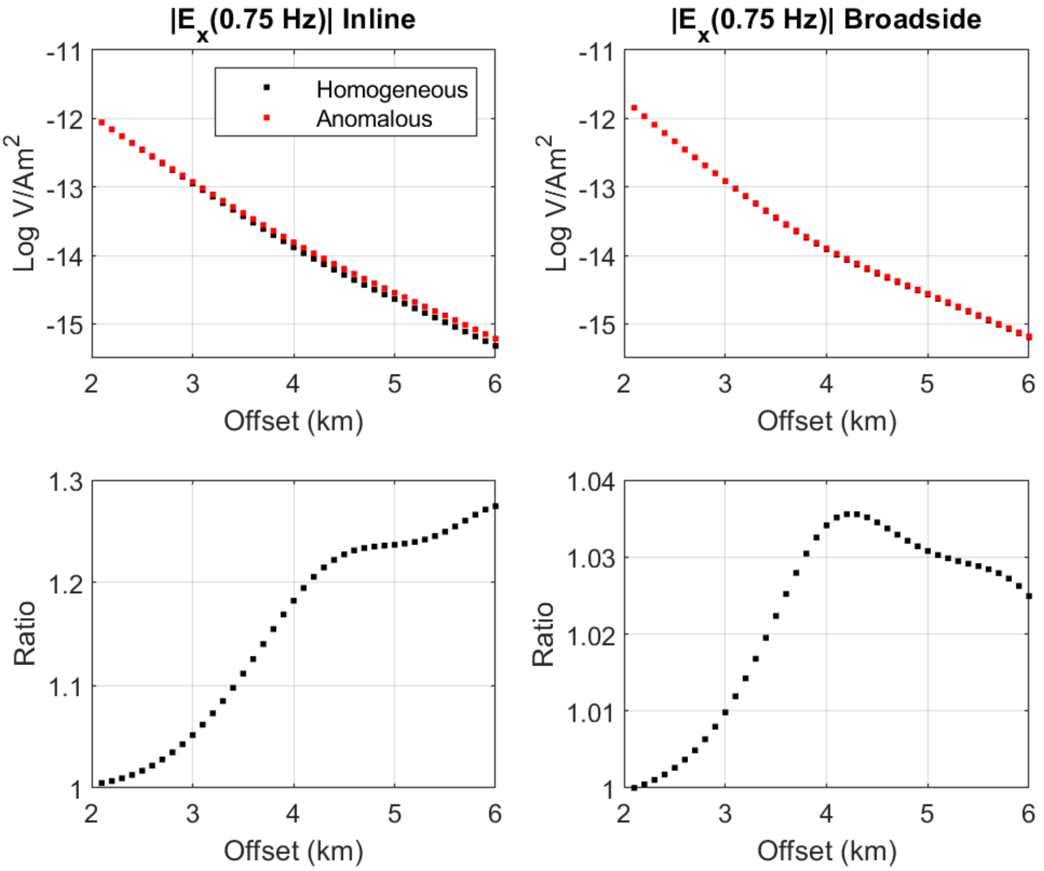

Figure 6 – Above, the CSEM inline and broadside electric fields at the chosen frequency and offsets, for homogeneous and anomalous IOI. Below are the corresponding ratios between the anomalous and homogeneous IOI responses.

The mathematical formulation of this composed model is approached in Appendix A. Appendix B calculates the analytical derivatives to build the Jacobian of petrophysical inversion [44] and related to the rock-physics parameters used to the petrophysical model calibration [45].

The rock-physics modeling of resistivity Res considers the porosity Φ, water saturation S_w, shale volume V_{sh}, tortuosity a, water resistivity $Resw$, shale resistivity $Ressh$, cementation exponents m and msh, and fluid exponents n and nsh:

$$1/Res = \frac{\Phi^m S_w^n}{aRes_w} + \frac{V_{sh}^{msh} S_w^{nsh}}{Res_{sh}}, \tag{2.1}$$

including the exponent nsh (Figure 19) as a slight modification to the original Simandoux formula [46, 47]. As in the elastic model, the shale volume is part of the rock matrix.

The composed rock-physics modeling $t(r)$ has parameters that must be calibrated to each facies [32, 45]. This work uses analytical derivatives of $t(r)$ related to the inputs to efficiently build the Jacobian matrix T.

3 Sensitivity analysis (Motivation)

Below there are examples of the complementing aspects between seismic and CSEM signals in light of the inversion theory [34], which motivates the use of joint inversion for reservoir characterization.

The synthetic model of a reservoir generates the seismic and CSEM simulated data d_{obs} (contaminated with Gaussian noise as in Chapter 2) to be compared with the responses d_{scan} for scanning values of rock properties or the oil column thickness by the following normalized misfit function:

$$misfit = \sqrt{(d_{scan} - d_{obs})^T W_d (d_{scan} - d_{obs})/N}. \tag{3.1}$$

Where N is the number of data points and W_d is the inverse of the diagonal variance matrix C_d for the added noise in d_{obs}, in the cases of scanning geophysical rock properties $d_{scan} = g(m_{scan})$.

If scanning petrophysical properties $d_{scan} = g(t(r_{scan}))$, it must include the uncertainty in rock-physics modeling: $W_d = (C_d + GC_{m_r}G^T)^{-1}$, where G is the Jacobian of geophysical modeling and C_{m_r} is a diagonal matrix with the squared errors from the rock-physics modeling calibration (Figure 19).

3.1 Synthetic model

The 1D synthetic model in Figure 7 represents an IOI with three homogeneous layers: a shale rock sealing an oil-saturated sandstone over another sandstone saturated with brine. The reference values of rock properties (Table 1) are rounded averages from well-logs of the test well (WT) further presented in Section 5.1.

Geophysical and petrophysical properties of the synthetic model							
Lithofluid facies	V_p (m/s)	V_s (m/s)	ρ (g/cm^3)	Res (Ωm)	Φ	S_w	V_{sh}
Shale	2600	1300	2.2	3.4	0.13	0.3	0.55
Oil sand	3000	1500	2.2	70	0.24	0.26	0.11
Brine sand	3100	1500	2.2	0.8	0.23	0.87	0.11

Table 1 – Table of synthetic model properties by lithofluid facies: V_p and V_s are compression and shear velocities respectively, ρ is density. Φ is porosity, S_w is water saturation and V_{sh} is shale volume (dimensionless values).

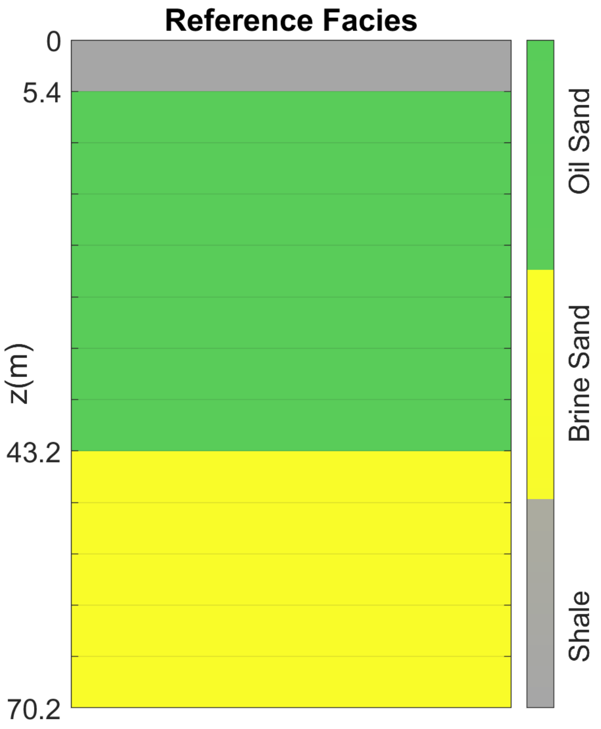

Figure 7 – Synthetic 1D model of a reservoir, z is depth relative to the top of the IOI, smooth gray lines are the 5.4 m discretization, and colors indicate the lithofluid facies.

3.2 Geometrical constraint

Figure 8 shows maps of the misfit function for scanning values of thickness h and V_p of the oil column, h only controls the depth of the oil-water contact. The 70.2 m-IOI, the shale layer, and all the not-scanned parameters are fixed on the reference values.

Seismic Misfit has a well-defined global minimum with coarsely circular surroundings, presenting a channel of h ambiguity for $misfit > 1.6$ and a local minimum for $h \approx 18$ m. CSEM Misfit with fixed Res shows less h resolution. However, CSEM data contributes to avoiding h ambiguity and local minima in Seismic+CSEM Misfit.

Figure 9 shows the same previous experiment framework, but fixing V_p and scanning Res. The region of ambiguity in CSEM Misfit with many local minima shows the well-known dominant sensitivity to the vertical transverse resistance $Res \times h$ [13, 40]. Thus, summing the seismic data better conditions h in CSEM+Seismic Misfit, which still presents a region of ambiguity, although weaker and with only global minimum.

A comparison between central maps in Figure 8 and 9 shows that seismic have superior resolution to h, not so far from CSEM.

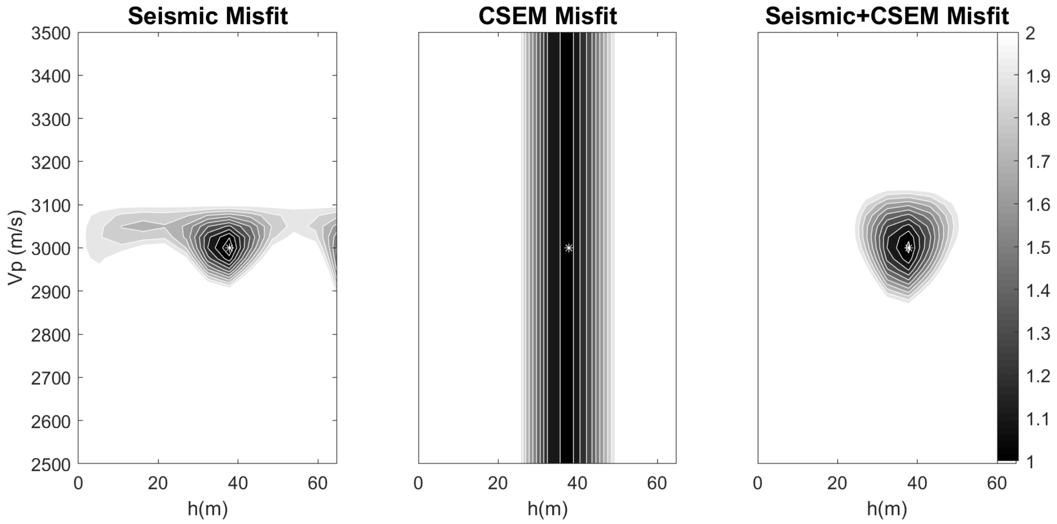

Figure 8 – Three maps of the misfit function varying the velocity Vp and thickness h of the oil column. At left for seismic stand-alone, at the center for CSEM with fixed *Res*, and right for the arithmetic average of the previous ones. The symbol * marks the reference values.

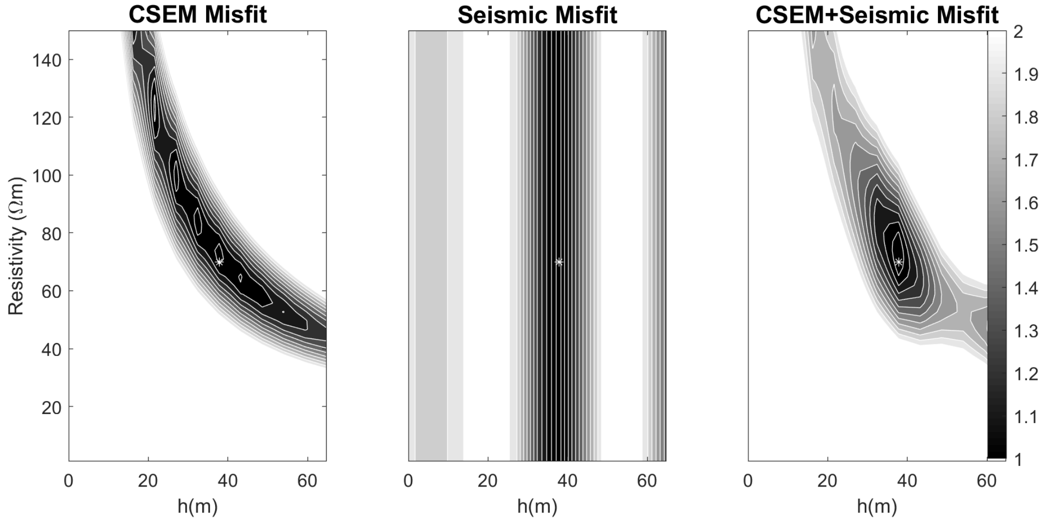

Figure 9 – Three maps of the misfit function varying the resistivity and thickness h of the oil column. At left for CSEM stand-alone, at the center for seismic with fixed Vp, and right for the arithmetic average of the previous ones. The symbol * marks the reference values.

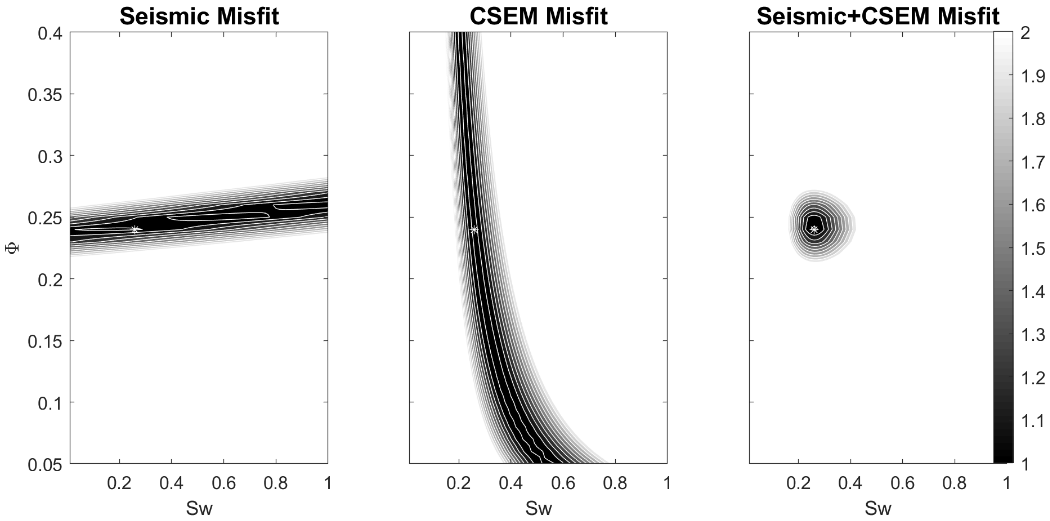

Figure 10 – Three maps of the misfit function varying the oil column's porosity Φ and water saturation Sw. At left for seismic stand-alone, at the center for CSEM stand-alone, and right for the arithmetic average of the previous ones. The symbol * marks the reference values.

3.3 Petrophysical constraints

Figure 10 shows the same as the previous experiment framework, now fixing the thickness in the reference value $h = 37.8$ m and scanning the petrophysical properties Φ and S_w. The rock-physics modeling $t(r)$ (see Section 2.4) is previously calibrated on oil sand WT well-logs (see Section 5.2) to generate all the geophysical properties for the seismic and CSEM modeling. The input shale volume is also with the reference value $V_{sh} = 0.11$.

The maps in Figure 10 assume the geophysical rock properties as a perfect mirror of petrophysical ones through the rock-physics modeling function to generate the synthetic model $m_{synthetic} = t(r_{synthetic})$, data $d_{obs} = g(t(r_{synthetic})) + C_d\epsilon$, and scanning responses $d_{scan} = g(t(r_{scan}))$. Where ϵ is the vector of normalized Gaussian noise.

Seismic shows much more sensitivity to Φ, while CSEM response is dominated by S_w. Hence, integrating signals in Seismic+CSEM Misfit presents a well-defined global minimum. The stand-alone applications present quasi-orthogonal ambiguities, leading to a well-defined minimum on the joint data map.

Including the misfit of rock-physics calibration C_{m_r} to either normalize the misfit $W_d = (C_d + GC_{m_r}G^T)^{-1}$ in equation 3.1 and contaminate the synthetic model of geophysical rock properties $d_{obs} = g(t(r_{synthetic})) + (C_d + GC_{m_r}G^T)\epsilon$ lead to the more inaccurate and imprecise mapping in Figure 11. Although biased, the association of both data presents a well-conditioned minimum in Φ, and S_w indicates the presence of oil.

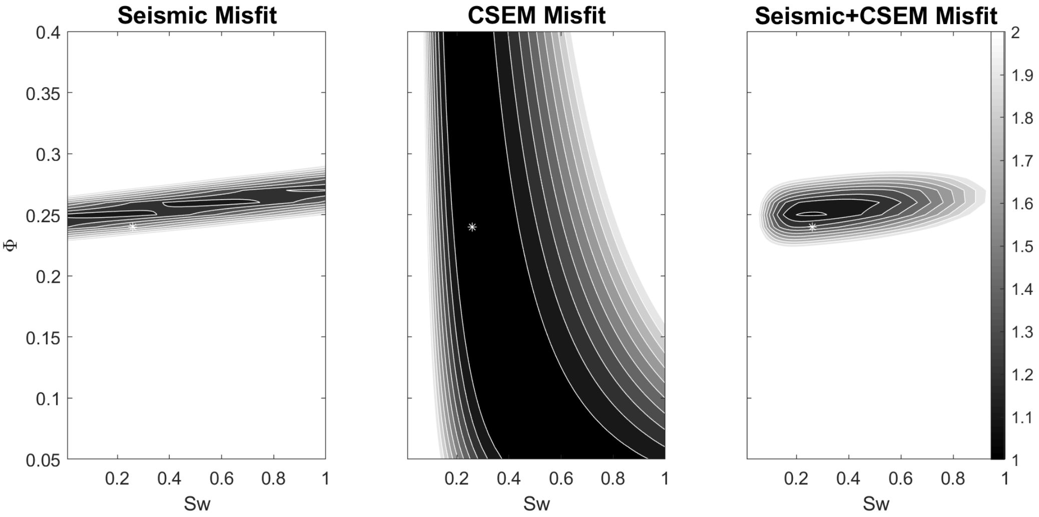

Figure 11 – Three maps of the misfit function varying the oil column's porosity Φ and water saturation Sw. At left for seismic stand-alone, at the center for CSEM stand-alone, and right for the arithmetic average of the previous ones. The data weight and added noise include the calibration misfit. The symbol * marks the reference values.

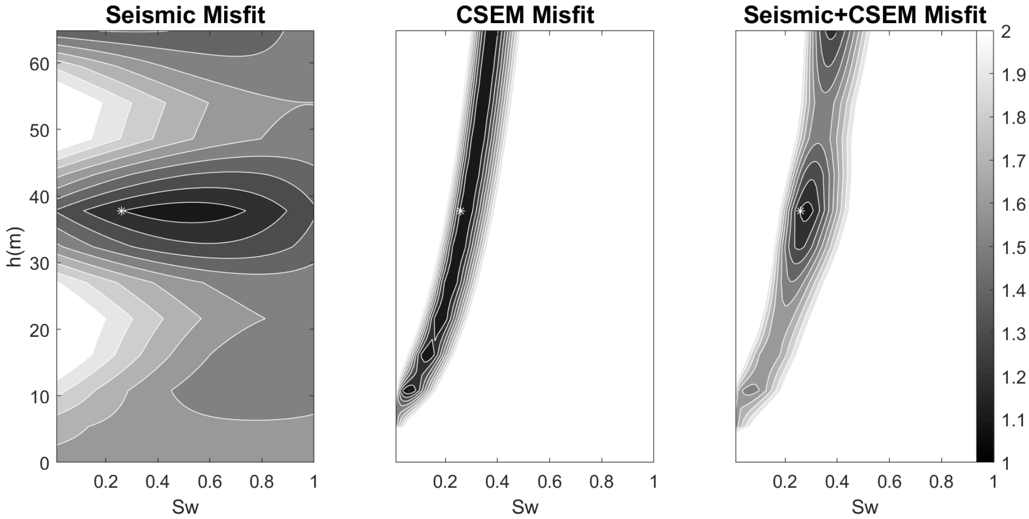

Figure 12 – Three maps of the misfit function varying the thickness h and water saturation Sw of the oil column. At left for the seismic stand-alone, at the center for the CSEM stand-alone, and right for the arithmetic average of the previous ones. The symbol * marks the reference values.

3.4 Geometrical and petrophysical constraints

Figure 12 shows the same as the previous experiment framework, now fixing $\Phi = 0.23$ and $V_{sh} = 0.11$ in the reference values and scanning S_w and h.

Seismic shows much more sensitivity to h, while CSEM response is dominated by S_w. These stand-alone applications present quasi-orthogonal ambiguities, which leads to a

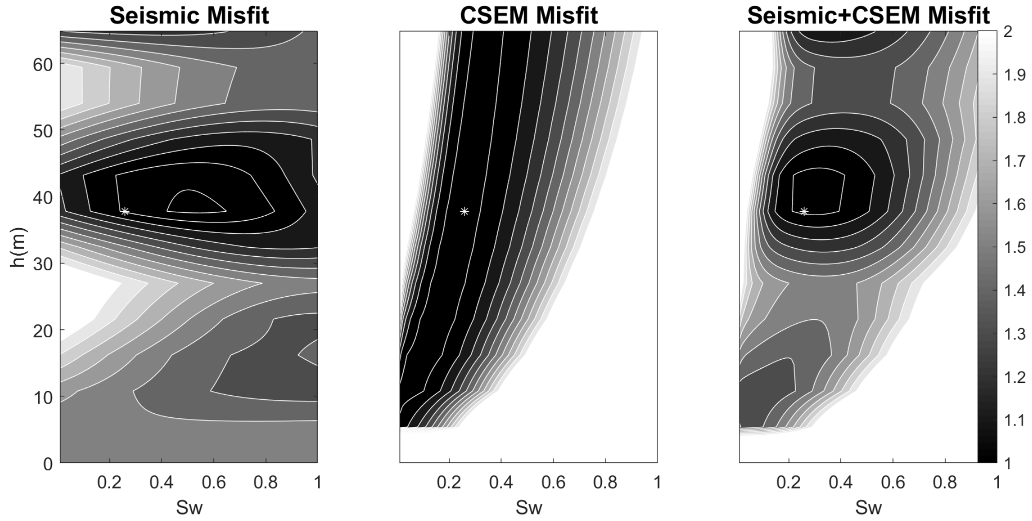

Figure 13 – Three maps of the misfit function varying the thickness h and water saturation Sw of the oil column. At left for the seismic stand-alone, at the center for the CSEM stand-alone, and right for the arithmetic average of the previous ones. The data weight and added noise include the calibration misfit. The symbol * marks the reference values.

better-defined minimum on the joint data map, although it presents a relevant region of ambiguity from CSEM.

Including the uncertainty in the rock-physics modeling leads to critical inaccuracy to h in all the maps but still provides a better definite minimum on the integration map (Figure 13), which at least indicates the presence of oil in S_w.

3.5 Partial conclusion

The association of seismic and CSEM minimizes or eliminates the ambiguities presented by stand-alone signals in experiments involving the geophysical rock properties, where only the geometry h constrains the elastic to resistivity models. In this case, simultaneous joint inversion for V_p and Res with a fixed h, for example, has no gain.

Conversely, although petrophysical properties couple elastic to resistivity models, the uncertainty in rock-physics modeling dramatically increases inaccuracy in mapping the target minimum.

This analysis demonstrates advantages in distinct associations of seismic and CSEM signals for reservoir characterization. Although the multiparametric inverse problem is far more complex than the exemplified maps, these experiments motivate us to approach geometrical, geophysical, and petrophysical constraints in the same inversion algorithm.

The following work proposes associating distribution modes of geophysical and petrophysical rock properties to lithofluid facies, then simultaneously inverting seismic and CSEM data to the same model composed by this categorical variable.

4 Methodology

This chapter discusses a Bayesian approach under Gaussian assumptions and linearized modeling for estimating the posterior probability density function (PDF) of the facies model within an interval of interest (IOI), including the proposed prior distribution that integrates geophysical and petrophysical rock properties, along with the numerical implementation of the theory using a Markov Chain Monte Carlo (MCMC) algorithm [33] for facies inversion. Calculating and implementing local inversions for rock properties are also presented as an optional subroutine.

4.1 Theory

The linearized Gaussian mixture technique for facies inversion [44] is generalized to combine two equivalent prior distributions on the marginalization integral, providing a hybridized analytical expression for the posterior facies likelihood.

4.1.1 Bayesian inferences

The desired posterior PDF $p(\pi|d)$ of the facies model π conditioned on the geophysical data d can be expressed by the following Bayesian inference [34]:

$$p(\pi|d) = \frac{p(d|\pi)p(\pi)}{p(d)}, \tag{4.1}$$

where $p(d|\pi)$ is the PDF for any possible geophysical data conditioned on a proposed facies model, and $p(\pi)$ is the PDF for any possible facies models and may be conditioned on prior information about facies spatial distribution within the IOI.

The term $p(d)$ normalizes the posterior distribution by the following summation over the entire space of possible facies configurations:

$$p(d) = \sum_{\pi \in \Omega^n} p(d|\pi)p(\pi), \tag{4.2}$$

such that for the model space $\Omega = \{\pi_1, \pi_2, ..., \pi_{n_f}\}$, the n_f discriminated facies arranged in n layers result in n_f^n possible configurations [28].

The PDF of the geophysical data conditioned on facies model $p(d|\pi)$ is given by the product of the data likelihood $p(d|m)$ with the prior distribution $p(m|\pi)$ marginalized in the m properties [6, 28]:

$$p(d|\pi) = \int p(d|m)p(m|\pi)dm. \tag{4.3}$$

Assuming Gaussian data noise and introducing the notation $(N_{data}(function, covariance))$ for Normal Distributions (ND) [4], the data likelihood of equation 4.3 can be written as:

$$p(d|m) = N_d(g(m), C_d) \equiv \frac{1}{\sqrt{\det(2\pi C_d)}} \exp\left[-\frac{1}{2}(d - g(m))^T {C_d}^{-1}(d - g(m))\right], \quad (4.4)$$

The prior PDF, $p(m|\pi)$, in equation 4.3 can be computed from the set of m properties (V_p, V_s, ρ and Res) directly acquired from well-log or core sample measurements for each facies. Thus, under the Gaussian assumption, it can be written as:

$$p_m(m|\pi) = N_m(\mu_m, C_m), \quad (4.5)$$

where μ_m is the vector of prior means and C_m is the prior covariance matrix. Although not indicated by subscripts for simplicity, all means, and covariances of rock properties are facies-related variables.

Alternatively, the prior PDF in equation 4.3 can also be computed from the petrophysical hard data r (Φ, S_w and V_{sh}) when it is transformed by a calibrated rock-physics modeling $m_r = t(r)$. In this case, the prior PDF of the transformed geophysical properties conditioned on facies takes the form of the following marginal distribution:

$$p_r(m|\pi) = \int p(m|r)p(r|\pi)dr. \quad (4.6)$$

Then, assuming both PDFs in equation 4.6 as NDs:

$$p_r(m|\pi) = \int N_m(m_r, C_{m_r})N_r(\mu_r, C_r)dr, \quad (4.7)$$

where μ_r is the vector of means, C_r is the covariance matrix of the r prior distributions, and C_{m_r} is a diagonal matrix with the squared errors of the rock-physics calibration, also assigned to each facies (Figure 19).

4.1.2 Proposed generalization

The following exponential balancing is now proposed to generalize equation 4.3 by including both priors of equations 4.5 and 4.7:

$$p(m|\pi) \propto {p_m}^{\alpha}(m|\pi){p_r}^{(1-\alpha)}(m|\pi), \quad (4.8)$$

where the parameter $0 \leq \alpha \leq 1$ weights each prior distribution type under the requirements of retrieving the stand-alone priors at the edges of this range and ensuring that α never decreases the covariances of either distribution, avoiding overfitting prior averages.

Thus, substituting equation 4.8 in 4.3 leads to the following generalized marginalization:

$$p(d|\pi) = \int p(d|m){p_m}^{\alpha}(m|\pi){p_r}^{(1-\alpha)}(m|\pi)dm. \tag{4.9}$$

4.1.3 Solving the integrals

To find an analytical solution for the marginalizations (equations 4.7 and 4.9), the geophysical $g(m)$ and rock-physics modeling $t(r)$ must be linear functions. The following calculus assumes hypothetical linear functions $g_{Lin}(m) = g_0 + Gm$ and $t_{Lin}(r) = t_0 + Tr$ tentatively before substituting them with the nonlinear functions $g(m)$ and $t(r)$ for the final $p(d|\pi)$ in equation 4.23.

Hence, the petrophysical marginalization of equation 4.7 is found using the known solution for the convolution of two NDs, whose arguments are linearly dependent on the integration variable [48, 49]:

$$p_r(m|\pi) = \int N_m(t_0 + Tr, C_{m_r})N_r(\mu_r, C_r)dr = N_m(t_0 + T\mu_r, TC_rT^T + C_{m_r}). \tag{4.10}$$

The prior PDFs must be expressed as NDs by including the regularization exponents (α in equation 4.9) inside the arguments:

$$p_m(m|\pi)^{\alpha} = N_m(\mu_m, \frac{C_m}{\alpha}) \tag{4.11}$$

and

$$p_r(m|\pi)^{1-\alpha} = N_m(\mu_{m_r}, \frac{TC_rT^T + C_{m_r}}{1-\alpha}), \tag{4.12}$$

where $\mu_{m_r} = t_0 + T\mu_r$.

Now, the PDF for geophysical data conditioned on the facies model takes the form:

$$p(d|\pi) = A\int N_d(Gm, C_d)N_m(\mu_m, \frac{C_m}{\alpha})N_m(\mu_{m_r}, \frac{TC_rT^T + C_{m_r}}{1-\alpha})dm. \tag{4.13}$$

Thus, renaming $C_{\alpha}^{-1} = \frac{\alpha}{C_m}$, $C_{\beta}^{-1} = \frac{1-\alpha}{TC_rT^T + C_{m_r}}$ (inverse to include $\alpha = 0, 1$) and then applying the following product rule for two NDs depending on the same variable [48, 49]:

$$N_m(\mu_m, C_{\alpha}) \cdot N_m(\mu_{m_r}, C_{\beta}) = N_{\mu_m}(\mu_{m_r}, C_{\alpha} + C_{\beta}) \cdot N_m(\mu_{\eta}, C_{\eta}), \tag{4.14}$$

with the joint covariance

$$C_\eta = \Big[{C_\alpha}^{-1} + {C_\beta}^{-1}\Big]^{-1} \tag{4.15}$$

and average

$$\mu_\eta = C_\eta\Big[{C_\alpha}^{-1}\mu_m + {C_\beta}^{-1}\mu_{m_r}\Big]. \tag{4.16}$$

Hence, the combined prior distribution in equation 4.8 assumes the form:

$$p(m|\pi) = AN_{\mu_m}(\mu_{m_r}, C_\alpha + C_\beta)N_m(\mu_\eta, C_\eta), \tag{4.17}$$

where the normalization constant A must cancel the m-independent function:

$$A = 1/N_{\mu_m}(\mu_{m_r}, C_\alpha + C_\beta), \tag{4.18}$$

thus, the resulting $p(m|\pi)$ is a ND, as follows:

$$p(m|\pi) = N_m(\mu_\eta, C_\eta). \tag{4.19}$$

Therefore, the posterior distribution in equation 4.3 becomes:

$$p(d|\pi) = \int N_d(g_0 + Gm, C_d)N_m(\mu_\eta, C_\eta)dm. \tag{4.20}$$

The integral in equation 4.20 can again be solved as a convolution of linear dependent NDs (equation 4.10):

$$p(d|\pi) = N_d(g_0 + G\mu_\eta, GC_\eta G^T + C_d). \tag{4.21}$$

By renaming $g_{Lin}(\mu_\eta) = g_0 + G\mu_\eta$ and $C = GC_\eta G^T + C_d$, the final expression is found:

$$p(d|\pi) = N_d(g_{Lin}(\mu_\eta), C). \tag{4.22}$$

In the following, we substitute the nonlinear functions $t(r)$ and $g(m)$ in equations 4.16 and 4.22 because it may improve the accuracy. Substituting $\mu_{m_r} = t(\mu_r)$ in equation 4.16 and $g(\mu_\eta)$ in equation 4.22 adapts the nonlinear forward functions to $p(d|\pi)$:

$$\boxed{p(d|\pi) = N_d(g(\mu_\eta), C)}, \tag{4.23}$$

where C is the covariance matrix:

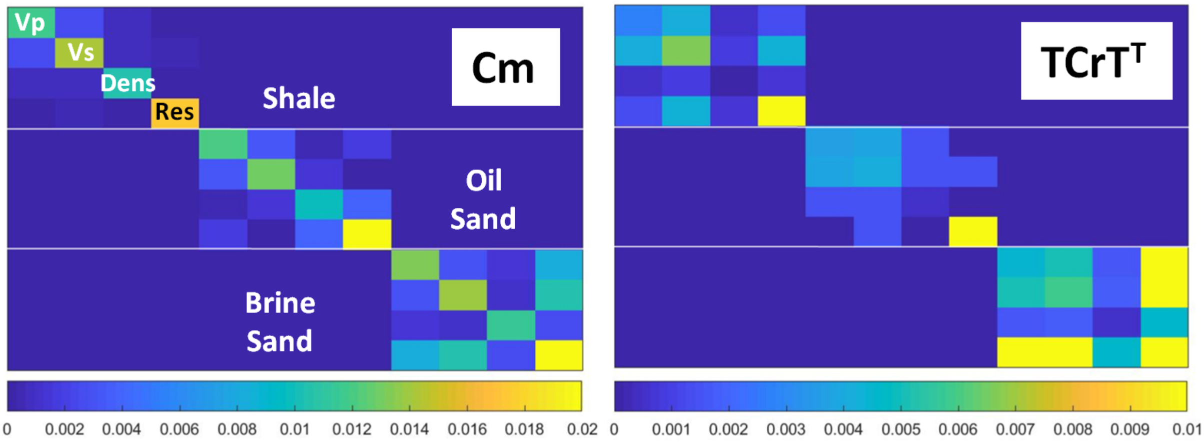

Figure 14 – Color map of covariance matrices Cm and $\mathrm{TCrT^T}$, for three layers model. Including the three chosen lithofluid facies (shale, brine sand, and oil sand), indicated on layers, and the four geophysical properties marked on elements of Cm picture (seismic velocities Vp and Vs, density Dens, and resistivity Res); and similar to $\mathrm{TCrT^T}$ picture.

$$\boxed{C = G\left[\frac{\alpha}{C_m} + \frac{1-\alpha}{TC_rT^T + C_{m_r}}\right]^{-1} G^T + C_d}. \tag{4.24}$$

The derivation of equations 4.23 and 4.24 can be validated by assuming the particular cases $\alpha = 0, 1$, as the same results are obtained by directly substituting $p_m(m|\pi)$ or $p_r(m|\pi)$ in equation 4.20, and then applying equation 4.10.

In equation 4.24, the precision (inverse of the covariance) matrices related to each type of prior distribution are summed, ensuring that in the middle of the range ($\alpha = 0.5$), the more accurate the information between the priors, the more significant its contribution to $p(d|\pi)$. This relevant aspect of the proposed equation 4.8 may also be attractive to other statistical applications.

After setting a realistic geological parametrization, the linearization and nonlinear adaptation are implicitly validated for the rock-physics modeling through the almost α-independent results in Section 5.3 and explicitly for the geophysical modeling in Section 5.4.

Figure 14 shows color maps of covariance matrices C_m and TC_rT^T, for a three layers model, each belonging to one of the three chosen lithofluid facies, with logarithmic values extracted from generic well-logs. The complementary between the covariances of each prior type is interesting for the inverse problem.

4.2 Implementation

This section presents the computational implementation for the proposed facies inversion and the local inversions for geophysical and petrophysical properties.

4.2.1 Facies from geophysical data

The analytical solution in equation 4.23 eliminates the need for numerical integration over the properties m (equation 4.3) for each facies configuration. However, the posterior distribution $p(\pi|d)$ (equation 4.1) can only be entirely determined by the evaluation of the product $p(d|\pi)p(\pi)$ over the whole facies model space Ω^n (equation 4.2), which may be numerically unfeasible. Therefore, an MCMC algorithm draws multiple facies realizations from this high-dimensional posterior distribution [6].

The probability for each proposed facies model $p(\pi)$ in equation 4.1 is assumed to be a first-order Markov Chain:

$$p(\pi) = p(\pi_1) \prod_{l=2}^{n} p(\pi_l|\pi_{l-1}), \tag{4.25}$$

where the facies probability at a given layer l depends on the adjacent facies at position $l-1$ according to the prior probabilities of facies occurrence $p(\pi_1)$ and transitions $p(\pi_l|\pi_{l-1})$. These probabilities are geological parameters based on prior knowledge about the spatial distribution of the facies in the IOI [24, 50].

At each iteration, a model window is randomly selected, keeping the same facies as the previous model in the top and bottom layers of the window. Then, the layers in between are perturbed using truncated Gaussian simulation, according to the matrix P, the elements of which are the facies transition probability between adjacent layers $p(\pi_l|\pi_{l-1})$ in equation 4.25. If the probabilities are uniformly applied over the layer pairs, P is a square matrix with a dimension equal to the number of facies [24]. This windowing is adopted to increase the acceptance rate compared to the perturbation of the entire model.

The geophysical rock properties are computed in logarithm scale and then concatenated on a vector by blocks related to each layer. Seismic and CSEM data are also concatenated into a data vector. The Jacobian and covariance matrices are built by layer-related blocks consistent with the rock properties vector.

After evaluating $p(d|\pi^{new})$ (equation 4.23) for the current model proposal, the acceptance rate is given by:

$$r = \min\{1, p(d|\pi^{new})/p(d|\pi^{last})\}, \tag{4.26}$$

where $p(d|\pi^{last})$ relates to the last accepted model.

Then, according to the Metropolis algorithm [6,33], a random number y with uniform distribution in the range $0 \leq y \leq 1$ is generated and compared to r. If $y \leq r$, the current configuration π^{new} is accepted. Otherwise, it is rejected, retaining the previous model (Figure 15). If accepted, the model sample is stored, along with its averages μ_η, responses $g(\mu_\eta)$, covariance C_η, Jacobians G and T, and π^{new} becomes π^{last} on the next iteration (Figure 15).

Despite $p(\pi)$ of equation 4.25 multiplies $p(d|\pi)$ in equation 4.1, it is not explicit in equation 4.26 because the described model perturbation implicitly introduces it.

In contrast with [6] and [23], no spatial correlation between layers is imposed on the covariance matrices to focus on the accuracy of each geophysical dataset under different prior settings and α effects (equation 4.8).

Beyond the burn-in period, stored samples provide a posterior distribution where the MAP is the most accepted model, and the uncertainties are extracted for each layer independently.

4.2.2 Local inversions

In the linearized Gaussian approach, geophysical and petrophysical rock properties can be estimated as conditional distributions by sampling local inversions over the accepted facies models [6,28]:

$$m \sim p(m|d,\pi) = N_m(\mu_{m|d,\pi}, C_{m|d,\pi}), \tag{4.27}$$

where the means and covariances conditioned on data and facies model for the proposed prior distribution (subscript η) are given by the following linear relations:

$$\mu_{m|d,\pi} = \mu_\eta + C_\eta G^T (G C_\eta G^T + C_d)^{-1} (d - G\mu_\eta) \tag{4.28}$$

and

$$C_{m|d,\pi} = C_\eta - C_\eta G^T (G C_\eta G^T + C_d)^{-1} G C_\eta. \tag{4.29}$$

However, under the assumed paradigm of using nonlinear forward functions, local inversions for rock properties achieve better adjustments through the following iterative process [14,34,35,51]:

$$\mu^{k+1}_{m|d,\pi} = \mu^{k}_{m|d,\pi} + C_\eta G_k^T (G_k C_\eta G_k^T + C_d + \lambda I)^{-1} \Big[d - g(\mu^{k}_{m|d,\pi}) + G_k(\mu^{k}_{m|d,\pi} - \mu_\eta) \Big], \tag{4.30}$$

where k is the iteration counter, $\mu^{0}_{m|d,\pi} = \mu_\eta$, λ is the Marquardt parameter (the starting value $\lambda = 0.01$ is empirically set), and I is the identity matrix [35,51]. The inversion stops when model changes reach a minimum value $|\mu^{k+1}_{m|d,\pi} - \mu^{k}_{m|d,\pi}| < \delta$. The covariance of the posterior properties $C_{m|d,\pi}$ is updated with the final Jacobian G_k in equation 4.29.

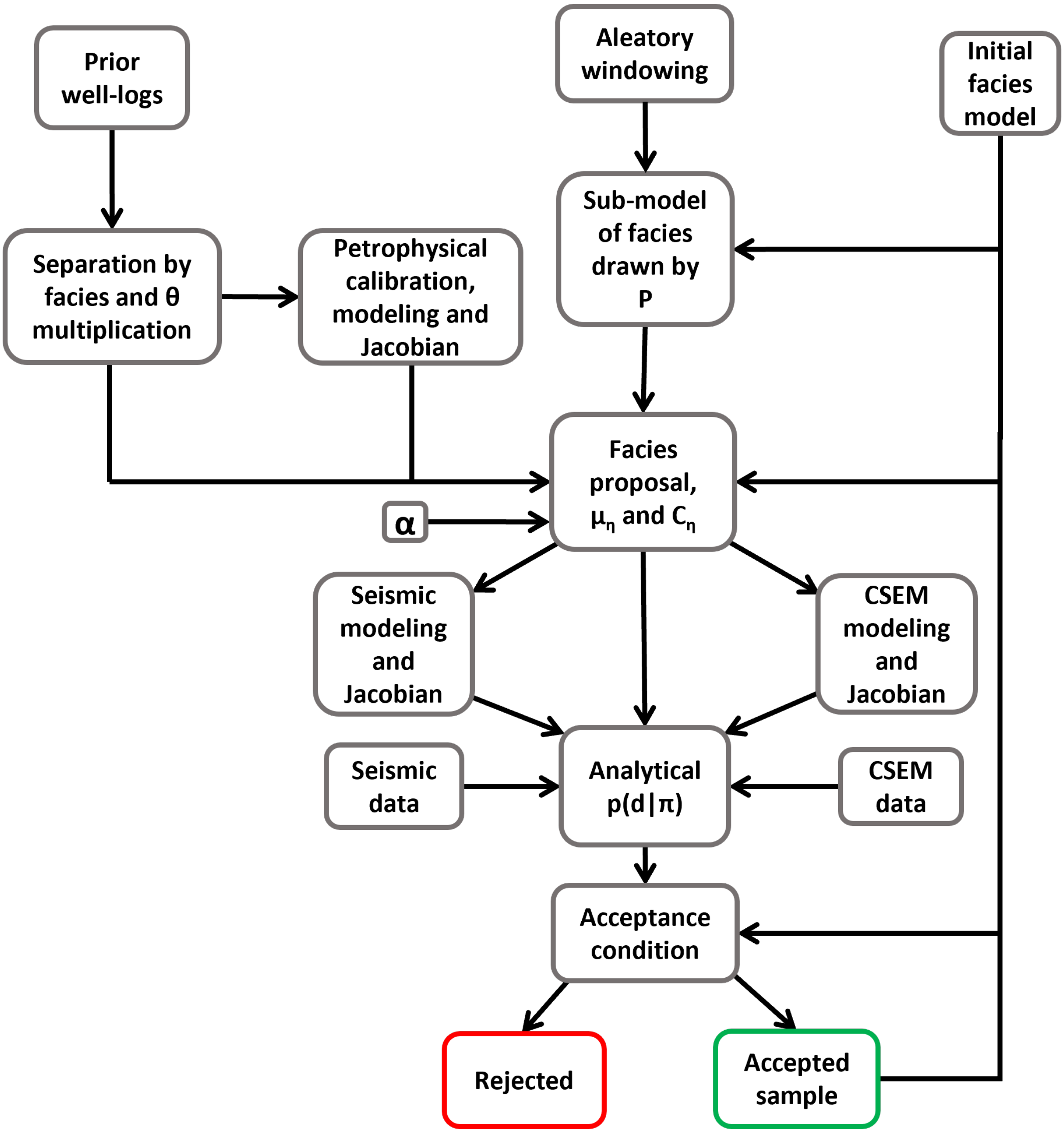
Prior well-logs
Aleatory windowing
Initial facies model
Separation by facies and θ multiplication
Petrophysical calibration, modeling and Jacobian
Sub-model of facies drawn by P
Facies proposal, μη and Cη
α
Seismic modeling and Jacobian
CSEM modeling and Jacobian
Seismic data
Analytical p(d|π)
CSEM data
Acceptance condition
Rejected
Accepted sample

Figure 15 – Block diagram for the facies inversion algorithm. Facies discriminate the rock properties from well-logs, and the electrical anisotropy ratio θ rescales the resistivities, calibrating rock-physics parameters to provide the misfit, means, and Jacobian for the geophysical transformed properties. The inputs are the means and covariances extracted from these treated prior well data, seismic and CSEM data, prior weight α, and the initial model. Seismic and CSEM modeling and Jacobians are the primary external functions of the looping. Aleatory widowing and facies sampling are subroutines with fixed parameters. The acceptance condition is based on MCMC. The accepted sample is inputted to build new facies proposal and stored to update the posterior distribution.

The same process is employed for the petrophysical properties $\mu_{r|m,\pi}$, by substituting d into the final $\mu_{m|d,\pi}$, the Jacobian G to T, C_η to C_r, C_d to C_{m_r} and similarly to its posterior covariance $C_{r|m,\pi}$. The properties r are limited within the critical limits by a logarithm barrier [52].

In this work, the two local inversions are done in cascade for quality control. However, the petrophysical properties could be directly inverted from the geophysical data by the composite function $g(t(r))$, changing μ_η and C_η to μ_r and C_r, G to GT and C_d to $C_d + GC_{m_r}G^T$ in equation 4.30, which has the advantage of coupling the elastic properties to resistivity and the disadvantage of not computing the geophysical rock properties.

To compute the posterior distribution $p(\gamma|d)$ of the rock properties $\gamma \in \{m, r\}$ (with m in logarithm and r in linear scale according to the inversion parametrization) an M-element (i-index) linearly spaced vector is created for each property γ and layer (with ranges that cover more than one standard deviation). The NDs $N_{\gamma_i}(\mu_{\gamma j}, C_{\gamma_j})$ are calculated with the means μ_{γ_j} and covariances C_{γ_j} given by local inversions for each accepted facies configuration represented by the j-index that includes repetitions in configuration acceptance. Thus, the average of those NDs over the j-index provides a M dimension posterior probability vector for each property and layer.

5 Data analysis

The inversion routine should be applied to a realistic geological scenario to assess the proposed hybrid prior modeling and the robustness of the inversion dealing with many different prior settings. Three wells of a marine reservoir were selected, one for the synthetic model and the others to provide the prior distributions.

This chapter presents the well data, the synthetic model by upscaling the test well profiles, the calibration of rock-physics parameters, the ability of the priors to predict the reference facies from the synthetic model of geophysical rock properties, surveying the full range of α, and a numerical validation for the nonlinear geophysical modeling adapted to the linearized Gaussian approach.

5.1 Well data

Three Maastrichian deep water reservoir wells (confidential geographic reference) were selected for this work: WP1, WP2, and WT, where (W) refers to the well, (P) to prior, and (T) to test. Each well contains the three lithofluid facies used in this work: shale, brine sand ($S_w \geq 0.5$), and oil sand ($S_w \leq 0.5$), the last two separated by the indicated oil-water contact (OWC), all inside the previously interpreted top and bottom of the IOI (Figure 16). Along the text, the convention to facies is 1-shale (gray), 2-brine sand (yellow), and 3-oil sand (green).

Notably, the resistivity of oil-saturated sandstone presents a high anisotropy ratio [53]. However, the conventional resistivity well-logs of the vertical wells employed are only sensitive to the horizontal resistivities Res_h. Meanwhile, the sensitivity of the employed isotropic CSEM modeling is dominated by the vertical resistivity Res_v [54].

As there is no triaxial induction well-log on these selected vertical wells [55], the ratio of electric anisotropy for each facies (θ_π) is coarsely estimated from horizontal wells and a fluid flow simulator on the reservoir [10]: $\theta_1 = 2$, $\theta_2 = 1.5$ and $\theta_3 = 10$. The vertical resistivity profiles are then computed by applying θ as a multiplicative factor on the resistivity data from the three wells (Figures 15 and 17). The fluid flow simulator also provides the effective pressure employed in the rock-physics modeling.

Figure 17 shows WT original and upscaled lithofluid facies with 13 layers of 5.4 m thickness each, determined by the adopted seismic time sampling, along with geophysical and petrophysical properties from WT well-logs, including the rescaled Res_v; the synthetic model, and the prior averages and standard deviations related to the upscaled facies model. The upscaling algorithm builds the synthetic rock properties model by averaging values

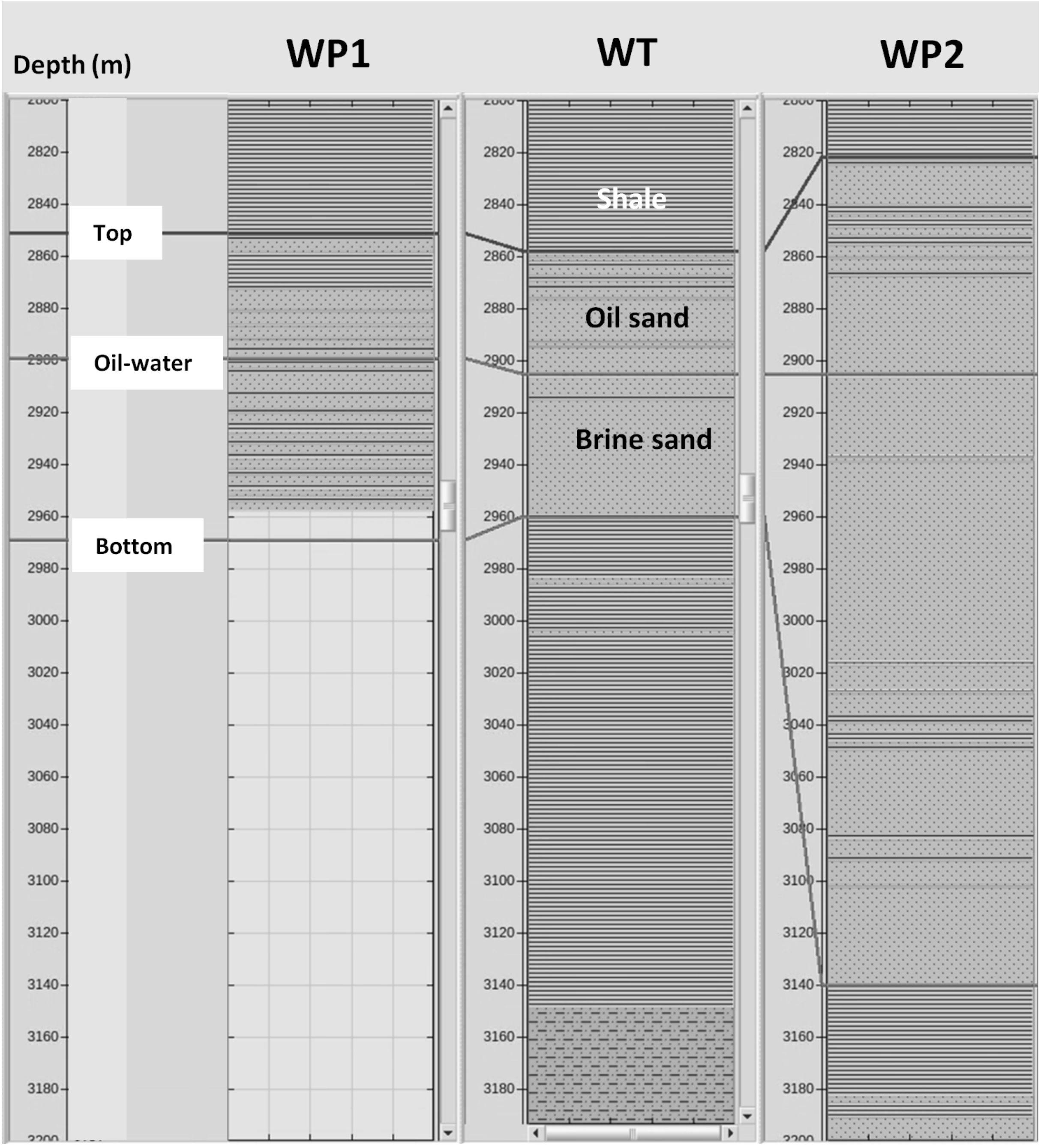
Depth (m)
WP1
WT
WP2
Top
Oil-water
Bottom
Shale
Oil sand
Brine sand
2820
2840
2860
2880
2900
2920
2940
2960
2980
3000
3020
3040
3060
3080
3100
3120
3140
3160
3180

Figure 16 – The lithological columns of prior wells (WP1) and (WP2), test well (WT) in depth. The lithofacies are indicated in textures without discriminating fluid saturation. The horizontal thickest lines indicate the top and bottom of the interval of interest (IOI) and oil-water contact (OWC) at each well.

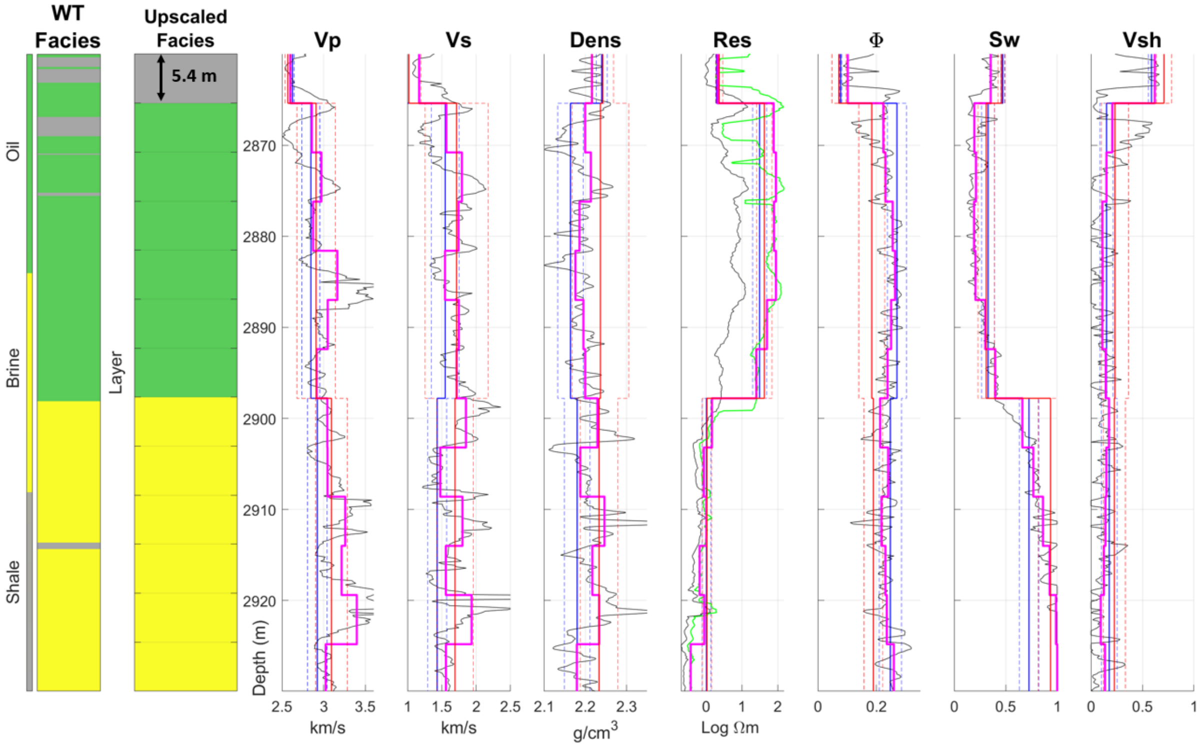

Figure 17 – The first two columns are the original and upscaled lithofluid facies of the WT in depth. The following frames are the rock properties profiles, with the original WT profiles in black, transformed vertical resistivity in green, and the synthetic model in magenta. Prior averages in blue lines for WP1, red lines for WP2, and dashed lines are their respective intervals of one standard deviation.

from the original profiles inside the respective upscaled layer. Quality control uses the inference method which will be described in Section 5.3 to ensure the synthetic model of geophysical rock properties has the most probability of belonging to the upscaled facies model.

In the following applications, the IOI top of the synthetic model is 2800 m as in Figure 3 (the original IOI top of WT is ≈ 2852 m in Figures 16 and 17), and the bottom is 2870.2 m, an interval corresponding to 13 layers of 5.4 m.

Figure 18 shows crossplots for the petrophysical properties V_{sh} versus Φ, elastic $I_s = \rho V_s$ versus acoustic $I_p = \rho V_p$ impedances, and vertical resistivity Res_v versus water saturation S_w, for WPs and WT. Each contour corresponds to one standard deviation of property pair distributions in multivariate form. The thinner contour lines are geophysical rock properties transformed from petrophysical properties by calibrated rock-physics modeling.

Shale presents sharp and poorly correlated distributions due to the shortage of well-log samples inside the IOI (Figure 16). To better characterize shale, it is necessary to complement the priors with well data samples outside the IOI limits, possibly discriminate

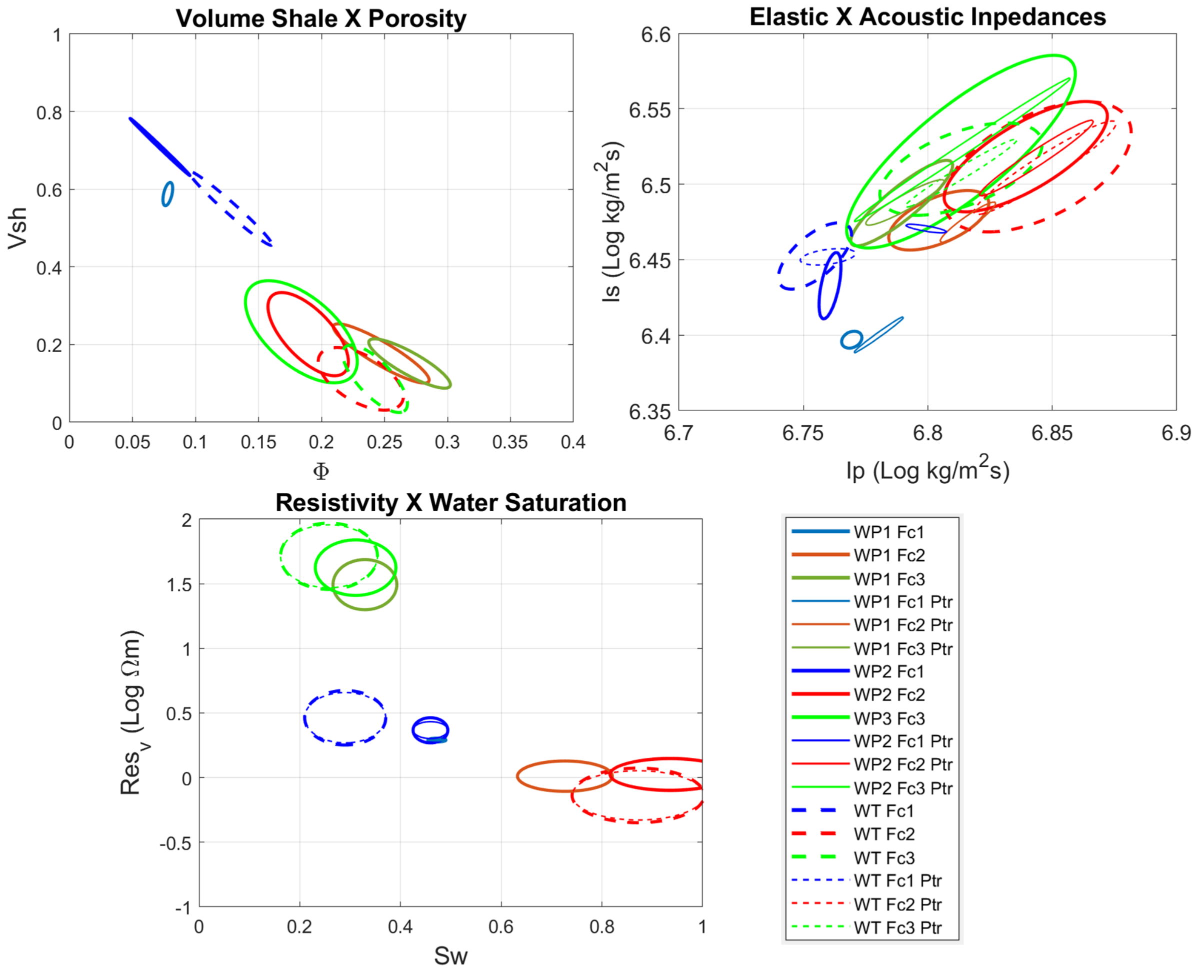

Figure 18 – Crossplots of shale volume Vsh versus porosity Φ, elastic Is versus acoustic Ip impedances, and vertical resistivity Res_v versus water saturation Sw. The contours correspond to one standard deviation for each pair of properties distribution related to facies, prior WPs, and reference WT wells. In legend, Ptr means that the corresponding geophysical property is transformed from petrophysical modeling.

shale in facies above and below OWC (Figure 16), and constrain its positioning by the transition matrix P (equation 4.25). However, the present application focuses on identifying the presence of oil and the OWC positioning.

There are possible challenges for the inversion, as some geophysical rock properties of the same facies are barely correlated between wells, i.e., shale I_s and Res_v between WPs and WT; also, some properties of distinct facies show superimposed distributions, i,e., I_p of brine and oil sands for the three wells.

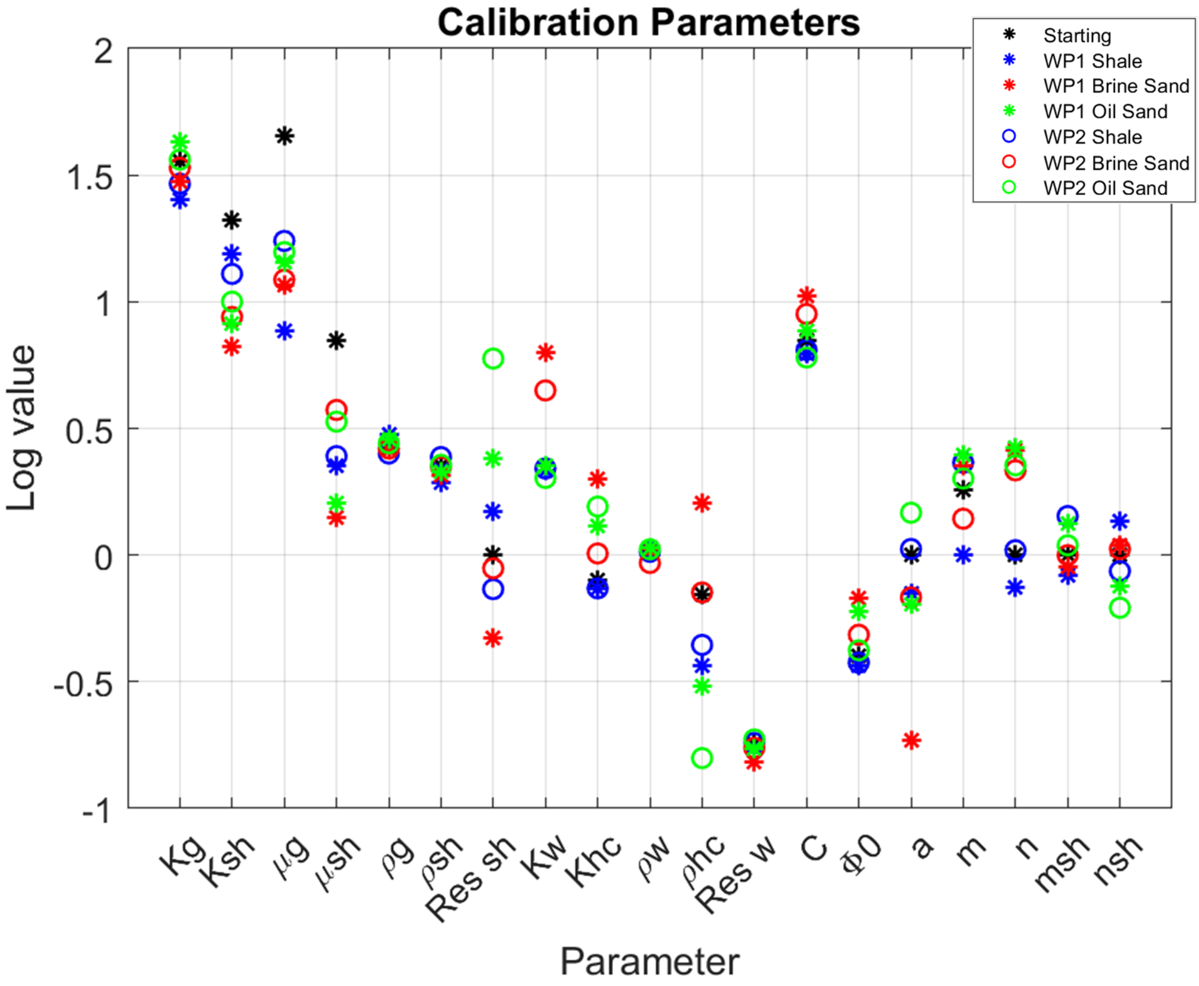

Figure 19 – Calibrated rock-physics parameters for each of the three employed facies and WP1 and WP2. Petroelastic parameters: the K and μ refer to bulk and shear moduli respectively, ρ to density, Res to resistivity, g to grain, sh to shale, w to water, hc to hydrocarbon, C to coordination number, Φ_0 to critical porosity. Petroelectric parameters: a is tortuosity, m and n are cementation and saturation exponents for grain and shale in the rock matrix.

5.2 Rock-physics calibration

Deterministic nonlinear inversion [34] calibrates the petrophysical modeling using the derivatives in Appendix B. All rock-physics parameters are inverted from the geophysical and petrophysical properties assigned to each facies in WP1 and WP2 well-logs, using a starting model with typical values for this environment (Figure 19).

The mean errors in the adjustment are about $2.4 - 3.8$ % for WP1 and $3.4 - 6.5$ % for WP2, depending on the facies. Figure 18 shows that most of the transformed elastic properties lie inside the hard data distributions except for WP shale due to the few samples and discrepancies in density profiles that lead to a poor fitting of densities, although not of velocities.

Figure 18 shows almost perfect fittings between measured and transformed resistivities because the water saturation well-log is calculated using the resistivity well-log. The contours are unskewed because, in the present approach, Res_v is uncorrelated to S_w in the prior covariance matrices, as they are properties of distinct kinds. The following methodology evaluates the most relevant aspects of these calibrations in light of the proposed inversion.

5.3 Facies from priors

The Bayesian approach is applied to infer the facies model from the synthetic model of geophysical rock properties under different priors as a quality control to support the interpretation of the subsequent geophysical modeling and inversions. Using averages and covariances of each WP and scanning α allow us to evaluate the correspondence between the priors and the synthetic model, the calibration of the rock-physics modeling, and the linearization.

Only the geophysical rock properties of the synthetic model are used as input for simulating geophysical data in further inversions. Thus, Bayes' rule for estimating facies conditional on properties m takes the form:

$$p(\pi|m) = \frac{p(m|\pi)p(\pi)}{p(m)}, \tag{5.1}$$

where $p(m|\pi)$ is given by equation 4.19, and $p(m)$ is a normalization factor as in equation 4.2.

Addressing the prior probability of facies occurrence and transitions is outside the scope of this analysis. Therefore, the inference is performed point-wise for each layer (l-index) with a uniform probability of facies occurrence and without setting any correlation between the layers. Thus, substituting equation 4.19 in equation 5.1:

$$p(i_l|m_l) = \frac{N_{ml}(\mu_{\eta_i}, C_{\eta_i})}{\sum_{i=1}^{3} N_{ml}(\mu_{\eta_i}, C_{\eta_i})}, \tag{5.2}$$

where the index i relates to facies ($i = 1$ is shale, $i = 2$ is brine sand, $i = 3$ is oil sand).

Hence, the MAP facies for each layer are determined by maximizing the facies probability for a given m_l:

$$i_l^{MAP} = \arg\max_i \{N_{ml}(\mu_{\eta_i}, C_{\eta_i})\}. \tag{5.3}$$

Figure 20 shows the facies models inferred by the described method from both WPs Elastic, Electric, and Joint rock properties for 11 α values regularly spaced in the $0 \leq \alpha \leq 1$ range.

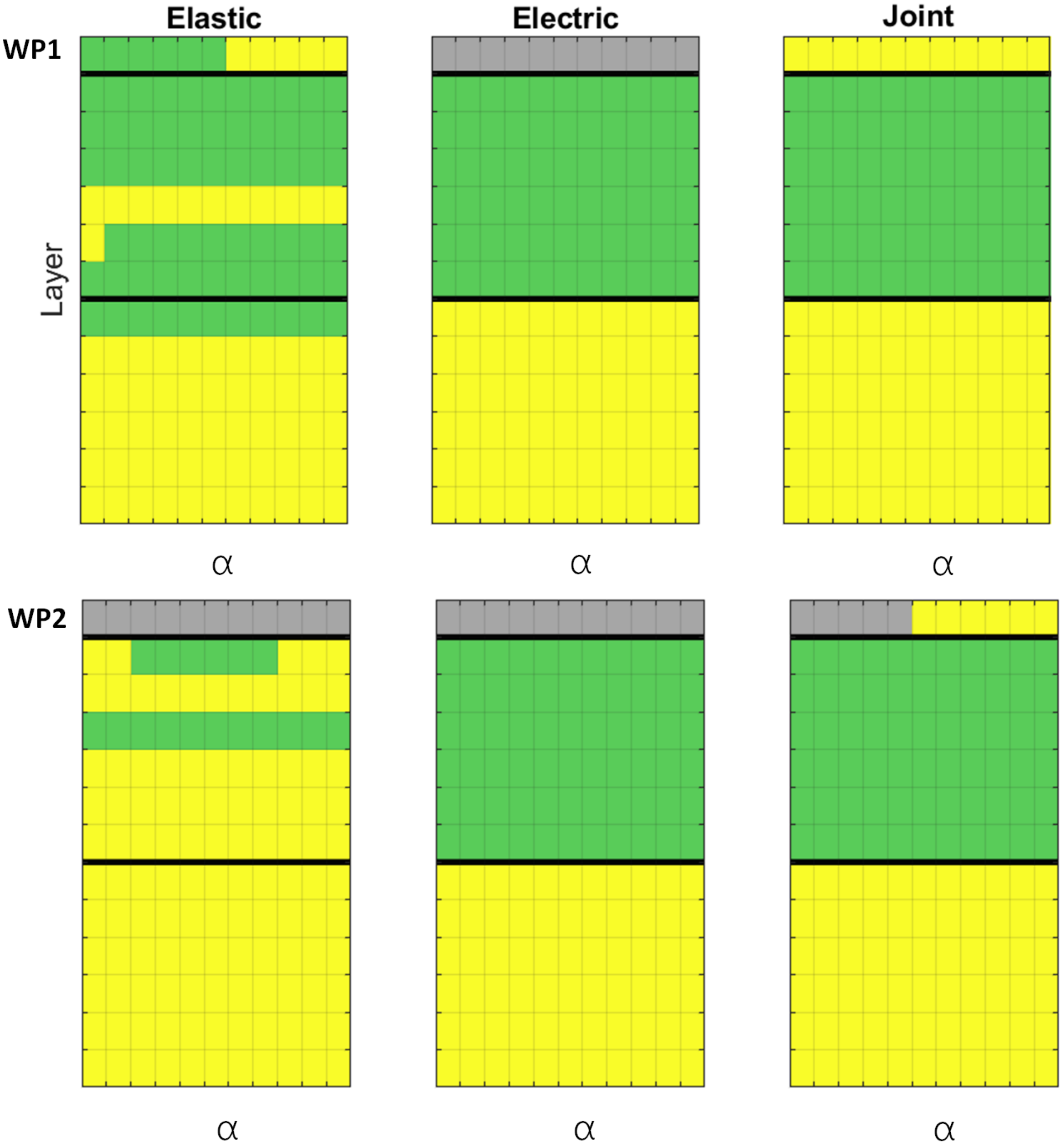

Figure 20 – Color map of 13-layer (y-axis) facies models inferred by applying the WP1 and WP2 priors over the synthetic model of geophysical rock properties. Frames for elastic-only (Elastic), resistivity-only (Electric), and (Joint) rock properties present a sequence of 11 inferred facies models related to α values regularly spaced between $0 \leq \alpha \leq 1$ (x-axis). Black lines are the reference facies transitions.

The results show that WP1 priors overestimate the oil column in elastic, retrieve the reference facies in electric, and retrieve the reference oil column in joint plots. The WP2 applications also retrieve the reference facies in electric and the reference oil column in joint plots. In opposition to WP1, the elastic plot in WP2 shows an underestimated oil column. These results support the worth of using resistivity to map fluid variations.

In most cases, the resulting facies show weak dependence on α, which validates the proposed adaptation of nonlinear rock-physics modeling to the linearized Gaussian approach (equations 4.16, 4.15 and 4.23).

Although some of the above results present brine just above oil, constraining facies transitions through equation 4.25 will avoid such a physical inconsistency in subsequent inversions.

5.4 Geophysical linearization

In Subsection 4.1.1, the geophysical modeling is assumed to be close to linearity surrounding the averages μ_η to achieve equation 4.23. Thus, the geophysical responses for the synthetic model of m properties are generated by the nonlinear functions for seismic $g^S(m_S)$ and CSEM $g^{EM}(Res)$ (see Sections 2.1 and 2.3), and compared with facies-related linear functions $g^S_{Lin}(m_S)$ and $g^{EM}_{Lin}(Res)$. In that analysis, the prior means and covariances are extracted from well-logs of WT itself (see Figures 17 and 18). It is limited to geophysical rock properties m ($\alpha = 1$ in equation 4.23) for assessing only linearization effects in geophysical modeling.

As discussed in Section 2.1, despite using Zoeppritz for modeling the reflection coefficients of seismic data, the Jacobian uses the Aki-Richards approximation [37], as follows:

$$g^S_{Lin}(m_S) = G_S \cdot m_S, \tag{5.4}$$

with m_S as the logarithm of the elastic properties and $G_S = S * AD$, where G_S is a function of $\mu_{Vp,Vs|\pi}$.

Meanwhile, CSEM linear modeling uses the exact analytical derivatives of nonlinear modeling (see [30] and Section 2.3) evaluated at $\mu_{Res|\pi}$, as follows:

$$g^{EM}_{Lin}(m_{EM}) = g^{EM}(\mu_{Res|\pi}) + G_{EM} \cdot (m_{EM} - \mu_{Res|\pi}). \tag{5.5}$$

Figure 21 compares the geophysical responses of the linear with the nonlinear modeling over the synthetic model for clear and contaminated signals. The difference

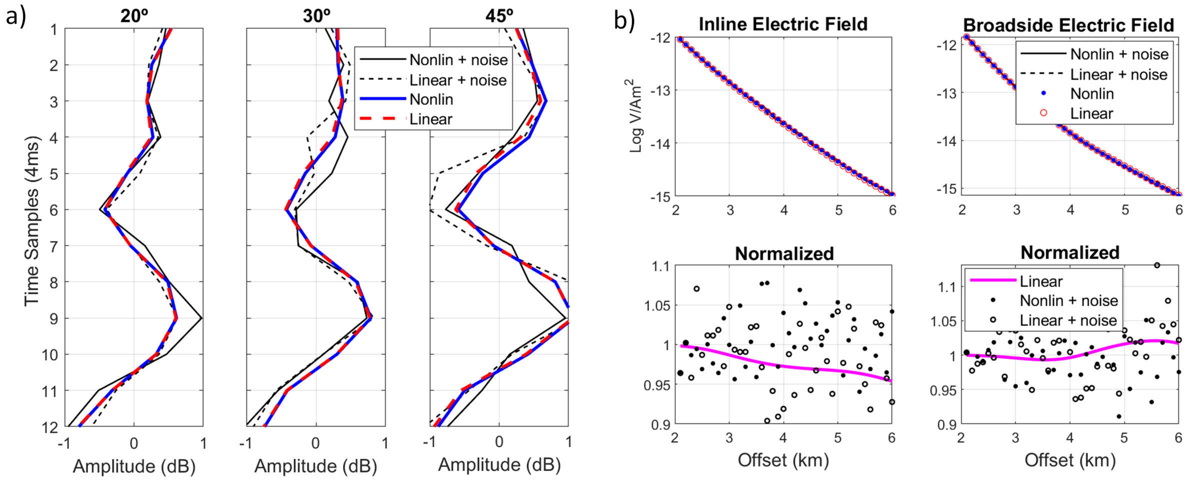

Figure 21 – Comparison between linear and nonlinear geophysical responses for the synthetic model: a) The three angle-related frames contain the seismic signals as indicated in the legend. b) The upper frames contain the CSEM inline and broadside signals; the clear nonlinear signal normalizes the others on the lower frames.

between the responses appears to be below the noise level for all datasets. However, the 5 % difference in the inline electric field at far offsets supports using the nonlinear function.

To compare the linear cases with the proposed nonlinear adaptation in $p(d|\pi)$ of equation 4.23, Figure 22 shows histograms for acceptance rates (see equation 4.26):

$$r = \min\{1, p(d|\pi^{trial})/p(d|\pi^{reference})\} \tag{5.6}$$

of trial facies models $p(d|\pi^{trial})$ against the reference facies model $p(d|\pi^{reference})$. The histograms represent the cumulative acceptance rates divided into 10 intervals between 0 and 1 for 100 simulated data d with different noise seeds in pictures for seismic and CSEM stand-alone and joint data for 13 trial models.

It is worth pointing out that seismic data uses the Aki-Richards approximation for the simulated data d_S and forward modeling $g^S_{Lin}(\mu_S)$ in the linear case and Zoeppritz for simulated data and forward modeling in the nonlinear case. In contrast, only the linearly generated d_{EM} is different from the nonlinear case, whereas the forward modeling is the same for both cases $g^{EM}_{Lin}(\mu_{Res}) = g^{EM}(\mu_{Res})$ (see equation 5.5).

These histograms for the probability of accepting a trial against the reference facies model are proposed as a simple way to assess the insertion of nonlinear modeling on the linearized Gaussian approach, as conceptually, it should be $r = 1$ for the correct trial model and $r = 0$ for the others. Although far from sampling the whole domain as the Bayesian inversion intends to do, comparing the posterior likelihood function for linear and nonlinear modeling and the resolution of each geophysical dataset in this way is

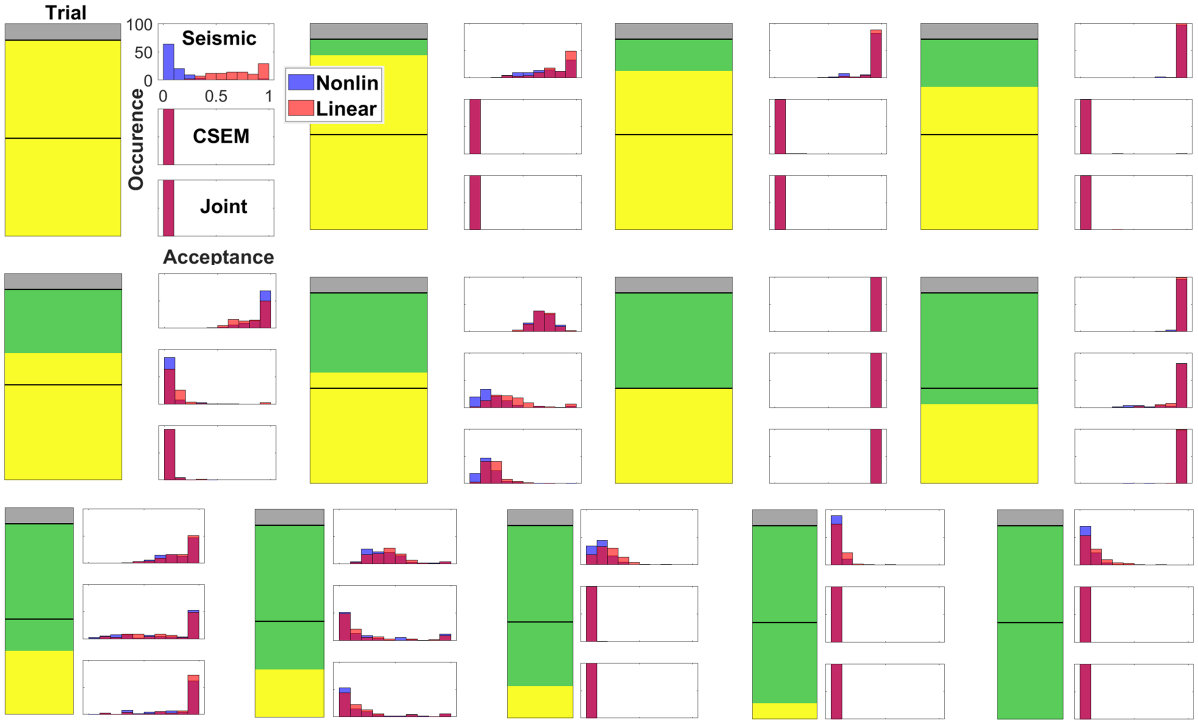

Figure 22 – Histograms of acceptance rate for 100 simulations per experiment based on a sequence of increasing oil column models for seismic and CSEM stand-alone and joint data. The blue bars are nonlinear, and the red bars are linear modeling, each covering a 0.1 acceptance rate interval. On the models, gray is shale, yellow is brine sand, green is oil sand, and black lines are the reference facies transitions.

enlightening.

The behavior of the histograms is generally similar for both functions, validating the nonlinear adaptation. Furthermore, the higher sensitivity to contrasts of the nonlinear modeling provides a more accurate acceptance rate for all displaced distributions in seismic and CSEM stand-alone and joint data.

These results clarify in advance that seismic difficulty in discriminating oil from brine sand and CSEM's tendency to overestimate the oil column on subsequent inversions are unrelated to adapting to the nonlinear forward functions on the linearized Gaussian approach.

Despite these results validating this application, performing similar numerical tests before running the inversion in other scenarios is recommended.

6 Applications and Discussions

The facies inversions are applied to synthetic data, scanning the α range for each prior well and geophysical dataset. Two possible challenges to CSEM are simulated: inversions for the lowest possible resistivity contrast and using a misleading overburden model.

The local inversions for rock properties are applied as a supplementary routine without scanning the prior settings or interpreting the results on the same level of detail as in the facies inversion.

As described in Section 4.2, the facies proposal distribution is introduced through stochastic perturbations conditioned on a transition probability matrix P (Figure 15). All inversions start from a homogeneous model of shale, the facies occurrence probability is uniform ($p(\pi_1) = \{1/3\}$ in equation 4.25), and the transition matrix P imposes a 90 % chance of choosing the same facies on the layer just below each one, 10 % of changing, and zero of placing oil just below a brine layer.

6.1 Inversion for facies

Figure 23 shows the MAP facies models inverted from contaminated geophysical data with a noise seed for each of 11 realizations using α regularly spaced values that cover the $0 \leq \alpha \leq 1$ range. These realizations are plotted side by side in frames of seismic (SS) and CSEM stand-alone (EM) and joint seismic/CSEM (SEM) inversions. The MAP facies model is the most accepted configuration in 2000 iterations, one order higher than the approximately 200 iterations of the burn-in period (Figure 30).

When comparing the inversions, SS applications show unstable and inaccurate results, contrasting with the EM. As the seismic signal is sensitive to the model contrasts, or differentiation, the CSEM signal is sensitive to the model integration (concept well expressed by the use of transverse resistance in [13], [14] and [12]), making it less susceptible to uncorrelated noise fluctuations. On the other hand, the integrative aspect of the CSEM signal impacts its resolution, tending to overestimate the oil column by stretching it up and down, also related to WP and α.

Fortunately, the SEM results meet the expectations about the complementarity of both geophysical methods when the contribution of the seismic data leads to more stable estimations than EM for the oil column, with an average bias of one extra oil layer below the reference OWC (Figure 23), regardless the prior settings. That means more reliability for reservoir interpretation and drilling risk assessment.

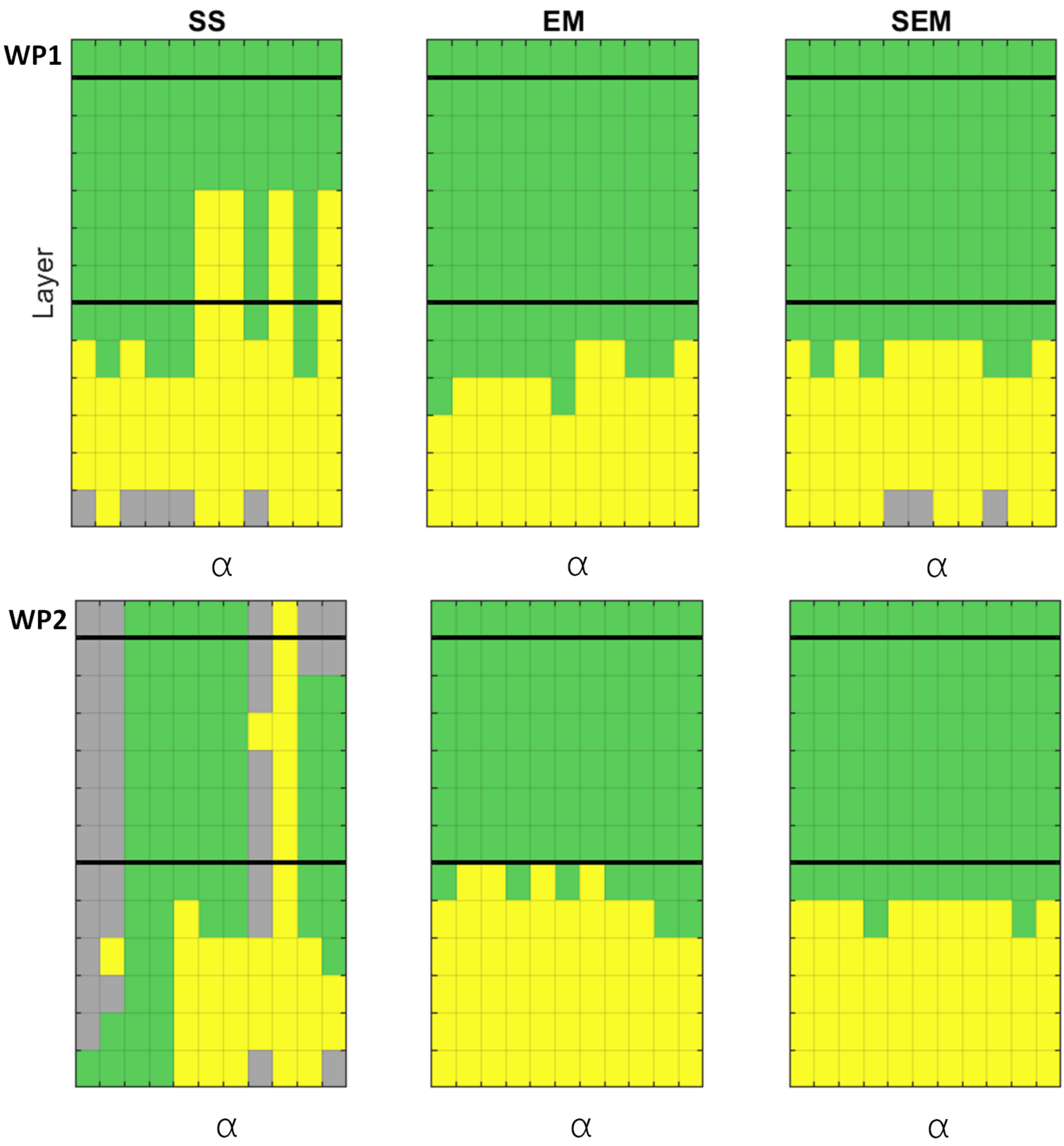

Figure 23 – Color map of 13-layer (y-axis) MAP facies models inverted geophysical synthetic data. Frames for seismic-only (SS), CSEM-only (EM), and joint inversions (SEM) present a sequence of 11 facies models related to α values regularly spaced between $0 \leq \alpha \leq 1$ (x-axis). Each inversion realization is applied to data with different noise seeds. Gray is shale, yellow is brine sand, green is oil sand, and black lines are the reference facies transitions.

6.2 Lower resistivity contrast

Multiplying the resistivity profiles of the three employed wells by the same anisotropy coefficients θ_π might be an artificial advantage of inverting simulated data. Hence, similar inversion experiments are performed with the original resistivities to assess the results without such an effect.

In Figure 24, inversion experiments that employ the original horizontal resistivities of WPs and WT (see Figure 17) present similar behavior to those with high anisotropy coefficients on the oil sand ($\theta_3 = 10$) in Figure 23, i.e., more stable OWC mapping in SEM than in EM inversions.

Although the higher the oil column resistivity, the higher the CSEM response, applications of vertical resistivity in Figure 23 retrieve worse OWC mapping than in Figure 24. This happens because the measured horizontal electric signal produced by the horizontal electric dipole is dominated by the transversal magnetic (TM) mode [56], which has a waveguide effect that concentrates the energy in the most resistive layers, shielding the sensitivity to the more conductive layers just below, as observed in Figure 22.

Aiming to support this argumentation, Figure 25 shows the 13 by 13 elements of sensitivity matrices [34] ratio $(G_c^T G_c)/(G_r^T G_r)$, where G_c and G_r are the CSEM Jacobians of the more conductive and the more resistive models, respectively. Note that the yellow squares (ratio above 1) are only related to the layers below the OWC, whose sensitivity is higher in the more conductive model.

The accurate SEM estimations for the oil column in Figure 24, ten times lower than the typical vertical resistivities in that environment (about 70 Ωm) [10, 12], indicate that the proposed methodology might work similarly to 3D body CSEM response, which is also lower than on employed 1D modeling [30].

6.3 Misguided overburden

Despite the prior and synthetic models based on well-logs, and the realistic noise added to the synthetic geophysical data, these controlled inversions have typical advantages over in-field applications: 1D isotropic approximations, exact acquisition parameters, the same IOI and discretization as the modeled data, which benefit both geophysical methods. The same background model and anisotropy ratio benefit CSEM, while the same wavelets and the Convolutional Model approximations (see Section 2.1) benefit seismic data.

Figure 26 shows a similar experiment. However, the CSEM simulated data is perturbed by a 10 Ωm-20 m layer, inserted 1000 m below the sea floor and 480 m above the IOI (see Figure 3) that is not introduced in the forward modeling, to simulate a pessimistic scenario, in which CSEM inversion model might bias the interpretation of the reservoir due

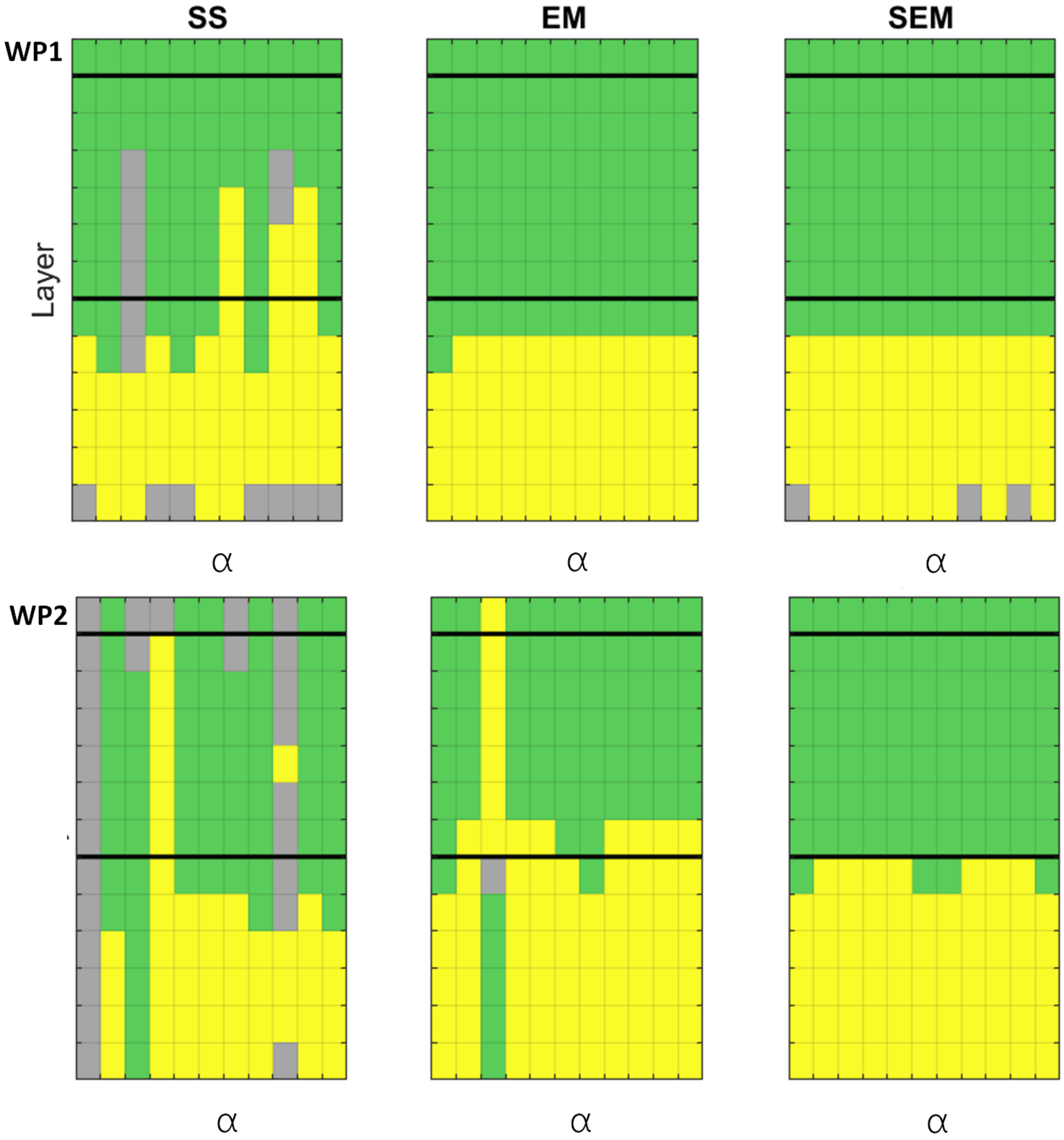

Figure 24 – Color map of 13-layer (y-axis) MAP facies models inverted from geophysical simulated data over the less resistive synthetic model Res_h. Frames for seismic-only (SS), CSEM-only (EM), and joint inversions (SEM) present a sequence of 11 facies models related to α values regularly spaced between $0 \leq \alpha \leq 1$ (x-axis). Each inversion realization is applied to data with different noise seeds. Gray is shale, yellow is brine sand, green is oil sand, and black lines are the reference facies transitions.

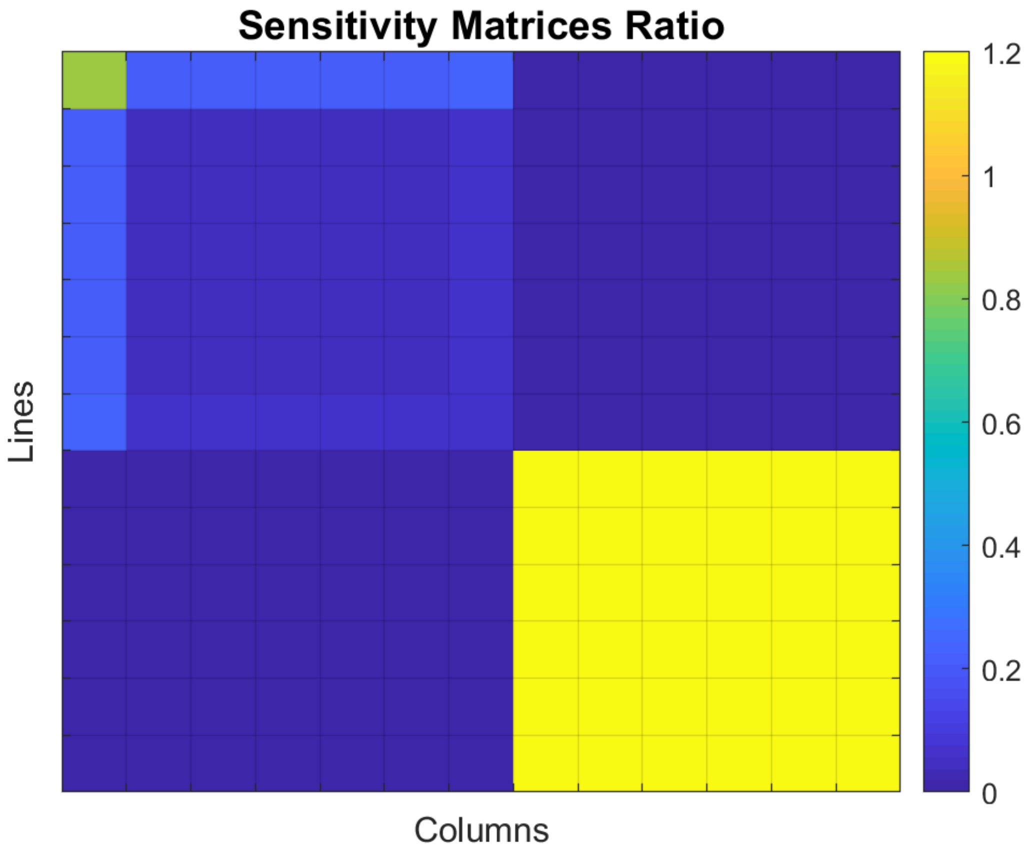

Figure 25 – Color map of 13 by 13 elements of the ratio between sensitivity matrices $(G_c^T G_c)/(G_r^T G_r)$, where G_c and G_r are the Jacobians of the more conductive more resistive models respectively.

to the presence of some unidentified resistive rock in the overburden [10], e.g., carbonates, gas hydrate, salt, igneous and volcanic rocks, and cemented sandstone.

In contrast with the previous results, EM and SEM inversions retrieve the oil column consistently overestimated by 4 to 6 extra oil layers below the reference OWC, showing that this anomalous resistive layer strongly impacts the CSEM signal and could introduce errors in its interpretation. However, penalizing the CSEM data fitting in SEM by incorporating a multiplicative factor to increase the corresponding variance elements in C_d (equation 4.24) allows the seismic signal to improve the OWC estimation (last frame in Figure 26).

Under the Bayesian approach, prior covariances control the weight of each rock property and geophysical data in the facies inversion and could be interpretation parameters as in the present case. For instance, [19] proposes balancing electromagnetic to seismic data by the ratio between starting model responses misfit.

Such an example suggests that the proposed simultaneous geophysical inversion could mitigate other sources of errors from each geophysical method.

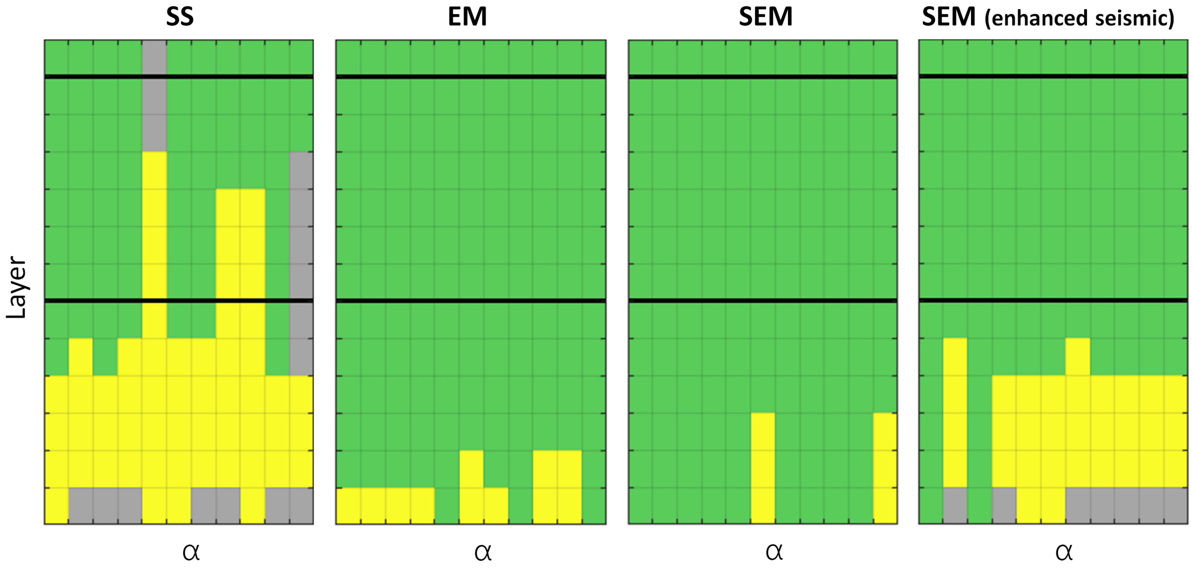

Figure 26 – Color map of 13-layer (y-axis) MAP facies models inverted from geophysical simulated data with CSEM perturbed by a resistive layer on the overburden. Frames for seismic-only (SS), CSEM-only (EM), joint (SEM), and SEM with enhanced seismic inversions present a sequence of 11 facies models related to α values regularly spaced between $0 \leq \alpha \leq 1$ (x-axis). Each inversion realization is applied to data with different noise seeds. Gray is shale, yellow is brine sand, green is oil sand, and black lines are the reference facies transitions.

6.4 Inversions for rock properties

Figures 27 and 28 show conditional distributions of geophysical and petrophysical rock properties built by sampling deterministic nonlinear inversions performed over the accepted facies models, as described in Subsection 4.2.2. Figure 27 uses WP1 as a prior, and Figure 28 uses WP2, both with $\alpha = 0.5$.

Figure 29 shows the same inversion experiment using profiles from WT to gather the prior distributions and calibrate the rock-physics modeling. As expected, these more likely prior inputs provided better estimations than those using WPs.

Figure 30 shows the misfit for each facies iteration on SEM-WP1 inversion of Figure 27 after the local inversions for geophysical $(d - g(m_k))^T {C_d}^{-1}(d - g(m_k))$ and petrophysical $(m_k - t(r_{k_r}))^T {C_{m_r}}^{-1}(m_k - t(r_{k_r}))$ rock properties. Figure 31 shows the respective geophysical data, sampled, and MAP responses.

The inversions for rock properties are presented as an extra application since they are an easily accessible by-product of the proposed facies inversion. However, approaching that at the same level of detail as the facies inversion would require many more experiments beyond the scope of this work.

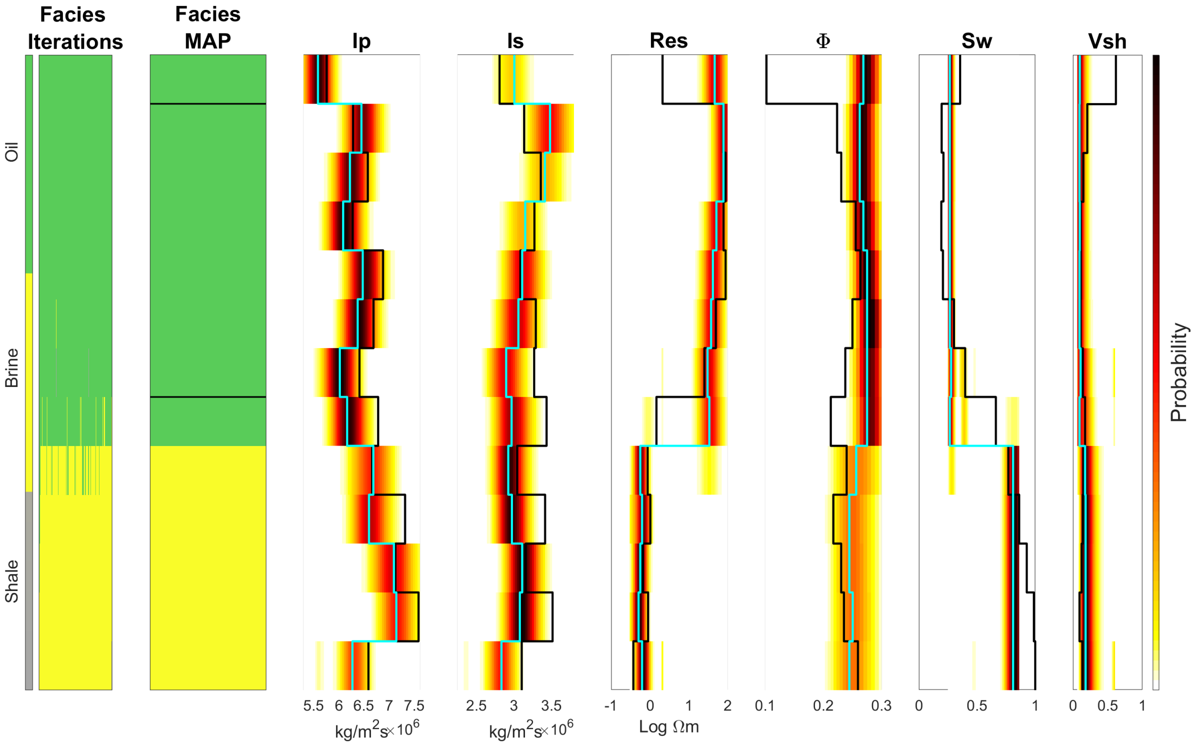

Figure 27 – Joint geophysical data inversion for facies, geophysical and petrophysical properties, with $\alpha = 0.5$ and priors from WP1. The first two columns are the facies iterations and MAP, and the black lines are the reference facies transitions. On the properties profiles, cyan lines are the MAP, color maps are the posterior probabilities, and black lines are the reference values.

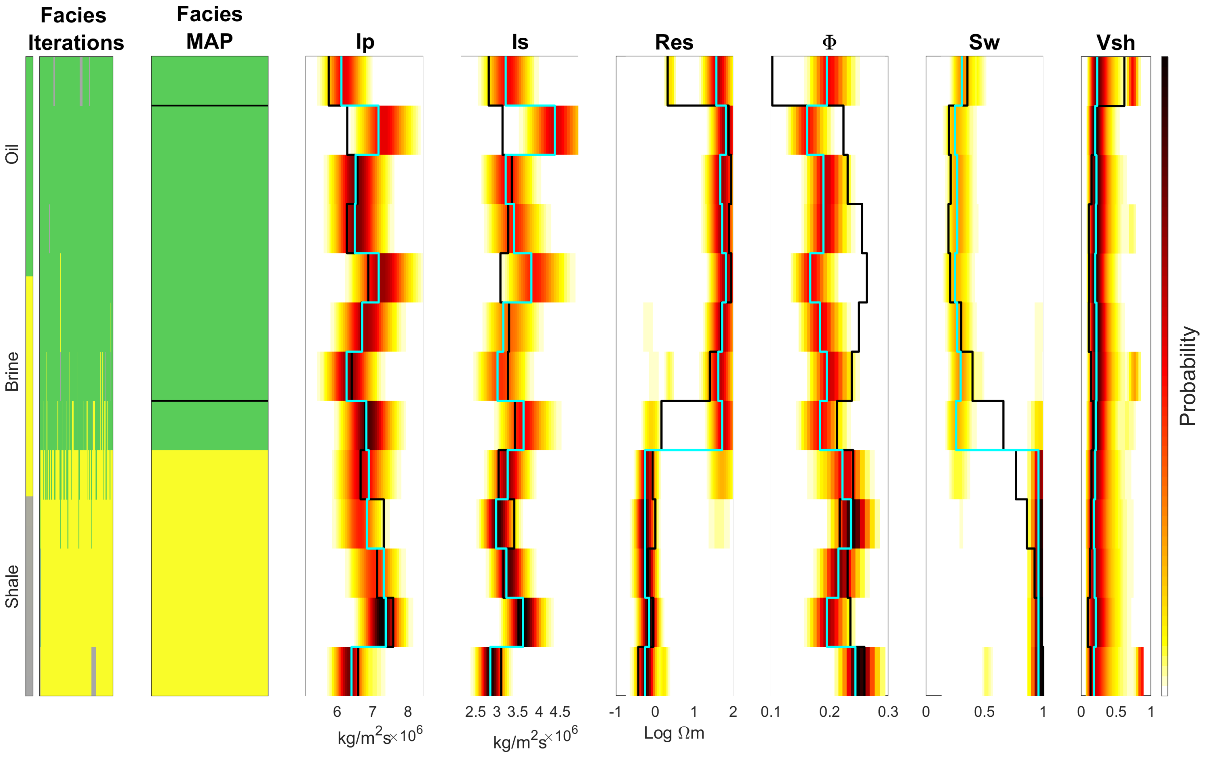

Figure 28 – Joint geophysical data inversion for facies, geophysical and petrophysical properties, with $\alpha = 0.5$ and priors from WP2. The first two columns are the facies iterations and MAP, and the black lines are the reference facies transitions. On the properties profiles, cyan lines are the MAP, color maps are the posterior probabilities, and black lines are the reference values.

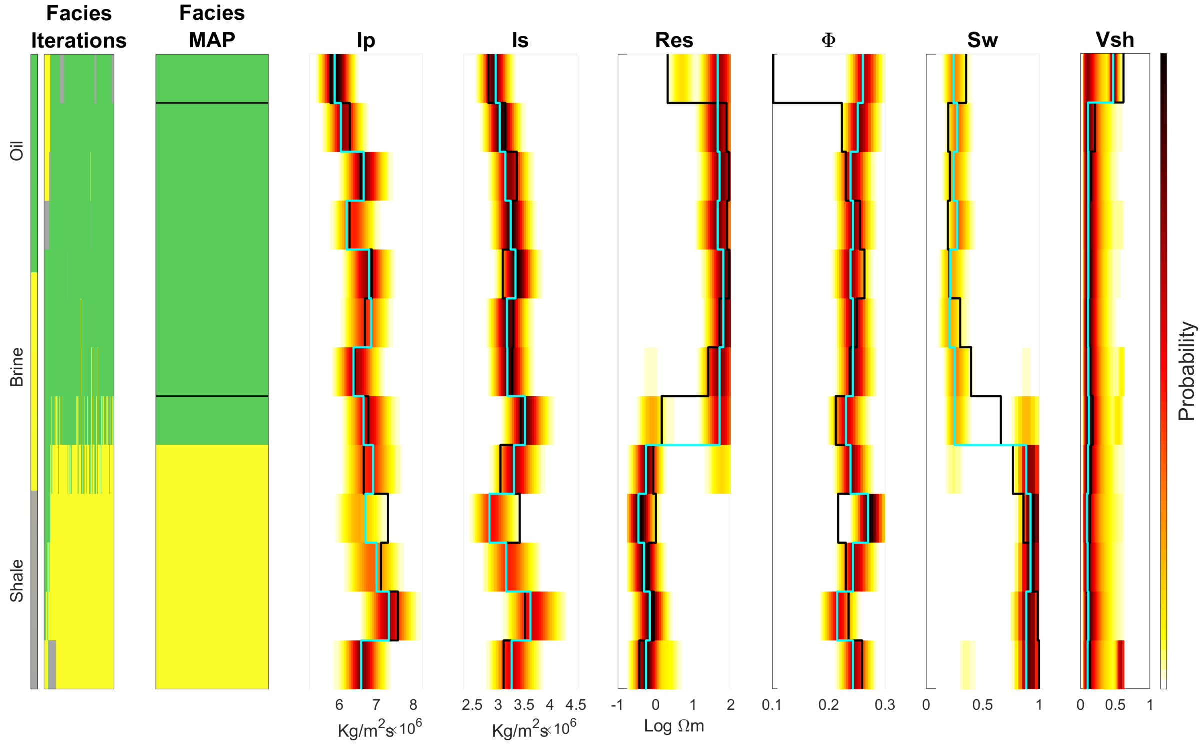

Figure 29 – Inversion for facies, geophysical and petrophysical properties, with $\alpha = 0.5$ and priors from WT. The first two columns are the facies iterations and MAP, and the black lines are the reference facies transitions. On the properties profiles, cyan lines are the MAP, color maps are the posterior probabilities, and black lines are the reference values.

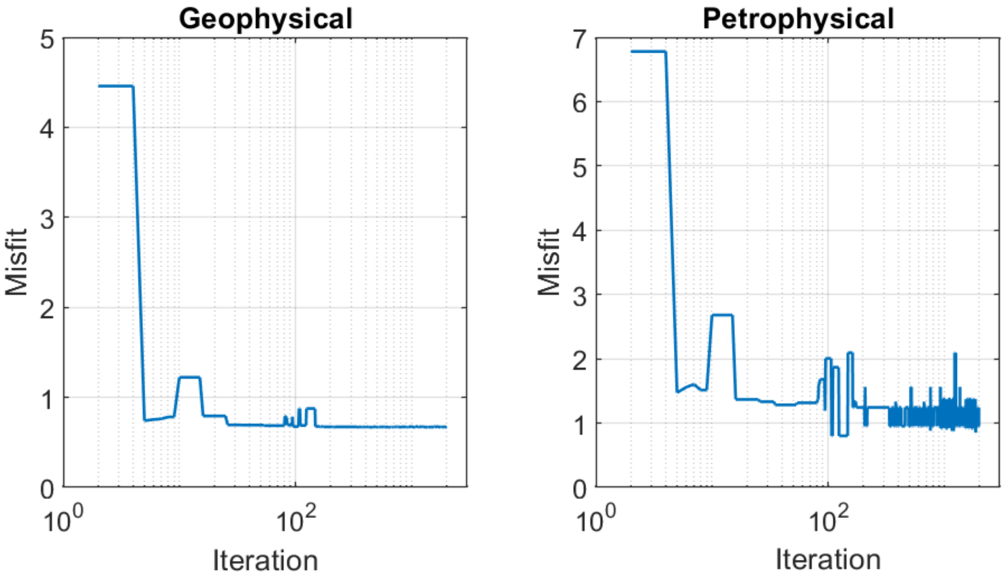

Figure 30 – Misfit evolution for geophysical and petrophysical local inversions in the 2000 facies iterations of joint geophysical data inversion, for WP1 with $\alpha = 0.5$.

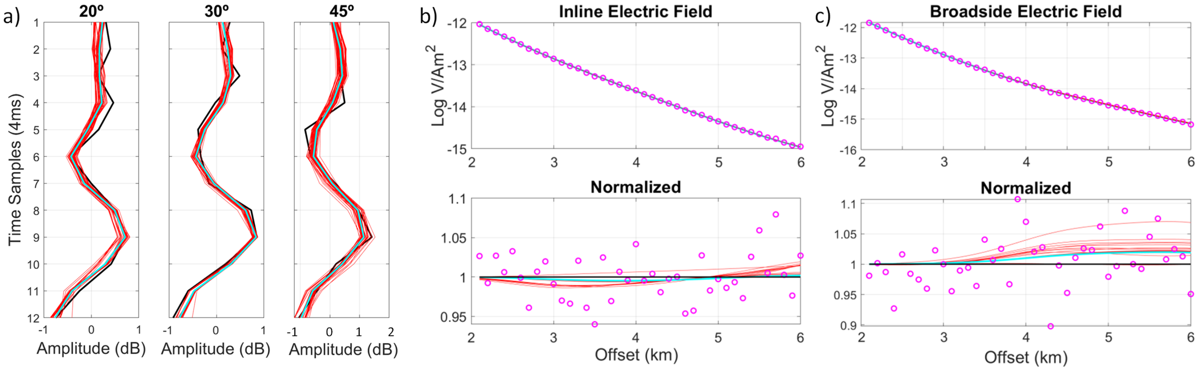

Figure 31 – Geophysical data and joint inversion responses: a) The frames separate seismic signals by the indicated angles with the contaminated data in black, the sample's responses in red, and the MAP response in cyan. b) The upper frames are CSEM inline and broadside electric contaminated data in magenta, the clear signal in black, the samples responses in red, and the MAP response in cyan; the lower frame is the same data normalized by the clear signal. c) The same as (b) for CSEM broadside signal.

7 Conclusion and Perspectives

The semi-analytical Bayesian algorithm successfully estimates models of lithofluid facies conditioned on seismic and CSEM data, including petrophysical and geophysical property distributions, weighted by an introduced parameter that allows us to test the inversions on many prior conditions.

The proposed generalization that associates two prior distributions in the same marginalization integral leads to an expression that prioritizes the most accurate information between them in the posterior covariance matrix. Such an aspect of this original approach might also be attractive for other applications.

The facies inversion is applied to well-based synthetic models with priors from one of two other wells per experiment, simulating scenarios of minimal information compared to what is usually available during the oil field recovery phase. Given that and the added noise, the results show that joint inversion for lithofluid facies can map vertical fluid variations in reservoir scale and robustly deal with noise and geological uncertainties in prior settings.

In stand-alone applications, the CSEM inversions provided stable oil column estimations inside subsets of prior information, in contrast with the general instability of the seismic inversions. However, the seismic influence on joint inversions stabilized the oil-water contact positioning, providing results weakly dependent on prior settings and data noise, always indicating the presence of oil with an average bias of two oil layers in addition to the six of the true model, with 5.4 m thickness each.

By comparing the inversion results with the incompatibilities between priors and elastic synthetic models previously observed by quality controls, the remaining deficiency of joint inversion to precisely map the oil column is CSEM resolution limitations and weak elastic response for fluid variations.

Two possible challenging scenarios for CSEM data inversion are also simulated. One with lower resistivity contrasts for fluid saturation provides better oil-water contact positioning because the less resistive oil column weakly shields the sensitivity to the lower layers.

In another scenario, the CSEM simulated data is perturbed by an anomalous resistive layer inserted in the overburden. However, as expected, the inversion background model omits this occurrence, leading to the CSEM inversion overestimating the oil column. However, joining the weight-enhanced seismic data improved the oil column estimation. That represents an example of difficult-to-access compensation for collaborative interpretation or multi-step joint inversion, justifying the simultaneous joint inversion and indicating that it can reduce other sources of uncertainty in stand-alone signal interpretations.

Assembling geophysical methods, rock properties, and prior information on the proposed semi-analytical facies inversion allows low-cost estimations of conditional distributions for geophysical and petrophysical rock properties. Although applied as a supplementary subroutine without testing many parametrizations, the results demonstrate potential for reservoir quantitative analysis, the quality of which depends on prior inputs.

Some other possible advances in this workflow are 1) optimizing α to condition the inverse matrices in facies and local inversions, 2) post-inversion optimization for the oil-water contact, 3) incorporate 3D CSEM and seismic modeling (i.e., finite-difference), 4) and include anisotropy as a rock property.

Appendix

APPENDIX A – Petroelastical model

Although well known, these mathematical models are presented to define the approach, sequence, and variables addressed in the subsequent calculation of derivatives.

General definitions

$\mathbf{\Phi}$ is porosity, **V** is volume, **S** is saturation, **K** is bulk modulus, μ is shear modulus, **P** is effective pressure.

Subscripts $_{\mathbf{g}}$ for grain, $_{\mathbf{sh}}$ for shale, $_{\mathbf{w}}$ for water, $_{\mathbf{hc}}$ for oil, $_{\mathbf{Vg}}$ for Voigt, $_{\mathbf{Rs}}$ for Reuss, $_{\mathbf{VR}}$ for Voigt-Reuss-Hill, $_{\mathbf{HM}}$ for Hertz-Mindlin, $_{\mathbf{dry}}$ for dry rock, $_{\mathbf{sat}}$ for saturated rock, and $_{\mathbf{fl}}$ for fluid.

Voigt-Reuss-Hill average

This is a simple way to define upper and lower bounds for effective elastic properties of a solid with two homogeneous phases.

Voigt model

The arithmetic average for bulk and shear moduli.

$$K_{Vg} = K_g(1 - V_{sh}) + K_{sh}V_{sh} \tag{A.1}$$

and

$$\mu_{Vg} = \mu_g(1 - V_{sh}) + \mu_{sh}V_{sh}. \tag{A.2}$$

Reuss model

The harmonic average for bulk and shear moduli.

$$K_{Rs} = \left[\frac{1 - V_{sh}}{K_g} + \frac{V_{sh}}{K_{sh}}\right]^{-1} \tag{A.3}$$

and

$$\mu_{Rs} = \left[\frac{1 - V_{sh}}{\mu_g} + \frac{V_{sh}}{\mu_{sh}}\right]^{-1}. \tag{A.4}$$

Voigt-Reuss-Hill average

The simple arithmetic average between both averages provides a generalized model that attends the Voigt upper and Reuss lower bounds for the moduli [8].

$$K_{VR} = 0.5(K_{Vg} + K_{Rs}) \tag{A.5}$$

and

$$\mu_{VR} = 0.5(\mu_{Vg} + \mu_{Rs}). \tag{A.6}$$

Hertz-Mindlin model

This model includes the geometry of grains and effective pressure.

For the defined Poisson Ratio

$$\nu = \frac{3K_{VR} - 2\mu_{VR}}{6K_{VR} + 2\mu_{VR}}, \tag{A.7}$$

$$K_{HM} = \left[\frac{C^2(1 - \Phi_0)^2 \mu_{VR}^2}{18\pi^2(1 - \nu)^2} P\right]^{1/3}, \tag{A.8}$$

and

$$\mu_{HM} = \frac{3(5-4\nu)}{5(2-\nu)} K_{HM}. \tag{A.9}$$

Where **C** is the **coordination number** of grain pack, which is related to the average number of contacts that each grain has with surrounding grains [8] and Φ_0 is the **critical porosity**.

Hashin–Shtrikman soft-sand model

It takes into account the porosity in effective elastic properties of dry rocks.

$$K_{dry} = \left[\frac{\Phi/\Phi_0}{K_{HM} + 4/3\mu_{HM}} + \frac{1-\Phi/\Phi_0}{K_{VR} + 4/3\mu_{HM}}\right]^{-1} - 4/3\mu_{HM}, \tag{A.10}$$

$$\mu_{dry} = \left[\frac{\Phi/\Phi_0}{\mu_{HM} + \xi} + \frac{1-\Phi/\Phi_0}{\mu_{VR} + \xi}\right]^{-1} - \xi, \tag{A.11}$$

with

$$\xi = \frac{\mu_{HM}}{6}\left(\frac{9K_{HM} + 8\mu_{HM}}{K_{HM} + 2\mu_{HM}}\right). \tag{A.12}$$

Hashin–Shtrikman stiff-sand model

It has the same format as the previous soft-sand model, but changing μ_{HM} to μ_{VR} in K_{dry} and the same change plus K_{HM} to K_{VR} in ξ.

Gassman model

It takes into account the pore fluids effect.

$$K_{sat} = K_{dry} + \frac{(1 - K_{dry}/K_{VR})^2}{\Phi/K_{fl} + (1 - \Phi)/K_{VR} - K_{dry}/K_{VR}^2}, \tag{A.13}$$

with the effective bulk modulus for the fluids mixture in porous space

$$K_{fl} = \left[\frac{S_w}{K_w} + \frac{1 - S_w}{K_{hc}}\right]^{-1}, \tag{A.14}$$

for water bulk modulus K_w and K_{hc} for oil.

As fluids have no shear resistance, μ remains μ_{dry}.

It is ignored a possible gas phase for a matter of simplification because some of the following expressions for derivatives are extensive, moreover it is easy to implement gas phase contribution for K_{fl} and ρ, by introducing the equation $S_w + S_{hc} + S_{gas} = 1$ [47]. In the presence of gas, it might be important to consider changes in K_{fl} due to changes in pressure [57].

Constitutive equations

Density

$$\rho = (1 - \Phi)\Big[(1 - V_{sh})\rho_g + V_{sh}\rho_{sh}\Big] + \Phi\Big[S_w\rho_w + S_{hc}\rho_{hc}\Big]. \tag{A.15}$$

Compression Velocity

$$V_p = \sqrt{\frac{K_{sat} + 4/3\mu_{dry}}{\rho}}. \tag{A.16}$$

Shear Velocity

$$V_s = \sqrt{\frac{\mu_{dry}}{\rho}}. \tag{A.17}$$

APPENDIX B – Jacobian of petroelastical model

In the same sequence as the previous formulation, the following calculus approaches the total derivatives of density and velocities as chain rules with the intermediate ones. Special notations are assumed to compress the expressions.

Derivatives of Voigt-Reuss-Hill averages $\mathbf{m_{VR}} = \{\mathbf{V_{sh}}, \mathbf{K_{g,sh}}, \mu_{\mathbf{g,sh}}\}$

$$\frac{dK_{VR}}{dV_{sh}} = 0.5\Big[K_{sh} - K_g + K_{VR}^2\Big(1/K_g - 1/K_{sh}\Big)\Big], \tag{B.1}$$

$$\frac{dK_{VR}}{dK_g} = 0.5(1 - V_{sh})\Big[1 + \Big(K_{Rs}/K_g\Big)^2\Big], \tag{B.2}$$

$$\frac{dK_{VR}}{dK_{sh}} = 0.5V_{sh}\Big[1 + \Big(K_{Rs}/K_{sh}\Big)^2\Big], \tag{B.3}$$

$$\frac{d\mu_{VR}}{dV_{sh}} = 0.5\Big[\mu_{sh} - \mu_g + \mu_{VR}^2\Big(1/\mu_g - 1/\mu_{sh}\Big)\Big], \tag{B.4}$$

$$\frac{d\mu_{VR}}{d\mu_g} = 0.5(1 - V_{sh})\Big[1 + \Big(\mu_{Rs}/\mu_g\Big)^2\Big] \tag{B.5}$$

and

$$\frac{d\mu_{VR}}{d\mu_{sh}} = 0.5V_{sh}\Big[1 + \Big(\mu_{Rs}/\mu_{sh}\Big)^2\Big]. \tag{B.6}$$

Derivatives of Hertz-Mindlin model

Poisson Ratio with respect to $\mathbf{m_{VR}}$

$$\frac{d\nu}{dm_{VR}} = \frac{\partial \nu}{\partial K_{VR}} \frac{dK_{VR}}{dm_{VR}} + \frac{\partial \nu}{\partial \mu_{VR}} \frac{d\mu_{VR}}{dm_{VR}},$$

with

$$\frac{\partial \nu}{\partial K_{VR}} = \frac{18\mu_{VR}}{(6K_{VR} + 2\mu_{VR})^2} \tag{B.7}$$

and

$$\frac{\partial \nu}{\partial \mu_{VR}} = \frac{-18K_{VR}}{(6K_{VR} + 2\mu_{VR})^2}. \tag{B.8}$$

Note that $\frac{dK_{VR}}{d\mu_{g,sh}} = \frac{d\mu_{VR}}{dK_{g,sh}} = 0$.

$\mathbf{K_{HM}}$ with respect to $\mathbf{m_{HM}} = \{\mathbf{m_{VR}}, \mathbf{P}, \mathbf{C}, \mathbf{\Phi_0}\}$

$$\frac{dK_{HM}}{dm_{HM}} = \frac{\partial K_{HM}}{\partial m_{HM}} + \frac{\partial K_{HM}}{\partial \mu_{VR}} \frac{d\mu_{VR}}{dm_{VR}} + \frac{\partial K_{HM}}{\partial \nu} \frac{d\nu}{dm_{VR}}, \tag{B.9}$$

with

$$\frac{\partial K_{HM}}{\partial \mu_{VR}} = \frac{2K_{HM}}{3\mu_{VR}}, \tag{B.10}$$

$$\frac{\partial K_{HM}}{\partial \nu} = \frac{2K_{HM}}{3(1-\nu)}, \tag{B.11}$$

$$\frac{\partial K_{HM}}{\partial P} = \frac{K_{HM}}{3P}, \tag{B.12}$$

$$\frac{\partial K_{HM}}{\partial C} = \frac{2K_{HM}}{3C} \tag{B.13}$$

and

$$\frac{\partial K_{HM}}{\partial \Phi_0} = -\frac{2K_{HM}}{3(1-\Phi_0)}. \tag{B.14}$$

$\mu_{\mathbf{HM}}$ with respect to $\mathbf{m_{HM}}$

$$\frac{d\mu_{HM}}{dm_{HM}} = \frac{\partial \mu_{HM}}{\partial m_{HM}} + \frac{\partial \mu_{HM}}{\partial \nu}\frac{d\nu}{dm_{VR}} + \frac{\partial \mu_{HM}}{\partial K_{HM}}\frac{dK_{HM}}{dm_{HM}}, \tag{B.15}$$

with

$$\frac{\partial \mu_{HM}}{\partial \nu} = -\frac{9K_{HM}}{5(2-\nu)^2}, \tag{B.16}$$

$$\frac{\partial \mu_{HM}}{\partial K_{HM}} = \frac{3(5-4\nu)}{5(2-\nu)}, \tag{B.17}$$

$$\frac{\partial \mu_{HM}}{\partial P} = \frac{\mu_{HM}}{3P}, \tag{B.18}$$

$$\frac{\partial \mu_{HM}}{\partial C} = \frac{2\mu_{HM}}{3C} \tag{B.19}$$

and

$$\frac{\partial \mu_{HM}}{\partial \Phi_0} = -\frac{2\mu_{HM}}{3(1-\Phi_0)}. \tag{B.20}$$

Derivatives of Hashin-Shtrikman soft-sand model

$\mathbf{K_{dry}}$ with respect to $\mathbf{m_{dry}} = \{\mathbf{m_{HM}}, \boldsymbol{\Phi}\}$

$$\frac{dK_{dry}}{dm_{dry}} = \frac{\partial K_{dry}}{\partial m_{dry}} + \frac{\partial K_{dry}}{\partial K_{VR}}\frac{dK_{VR}}{dm_{VR}} + \frac{\partial K_{dry}}{\partial K_{HM}}\frac{dK_{HM}}{dm_{HM}} + \frac{\partial K_{dry}}{\partial \mu_{HM}}\frac{d\mu_{HM}}{dm_{HM}}, \tag{B.21}$$

with

$$\frac{\partial K_{dry}}{\partial K_{VR}} = \left[\frac{K_{dry} + 4/3\mu_{HM}}{K_{VR} + 4/3\mu_{HM}}\right]^2 \Big(1 - \Phi/\Phi_0\Big), \tag{B.22}$$

$$\frac{\partial K_{dry}}{\partial K_{HM}} = \left[\frac{K_{dry} + 4/3\mu_{HM}}{K_{HM} + 4/3\mu_{HM}}\right]^2 \Phi/\Phi_0, \tag{B.23}$$

$$\frac{\partial K_{dry}}{\partial \mu_{HM}} = 4/3\Big[\frac{\partial K_{dry}}{\partial K_{VR}} + \frac{\partial K_{dry}}{\partial K_{HM}} - 1\Big], \tag{B.24}$$

$$\frac{\partial K_{dry}}{\partial \Phi} = \Big(K_{dry} + 4/3\mu_{HM}\Big)^2 \Big[\frac{1/\Phi_0}{K_{VR} + 4/3\mu_{HM}} - \frac{1/\Phi_0}{K_{HM} + 4/3\mu_{HM}}\Big] \tag{B.25}$$

and

$$\frac{\partial K_{dry}}{\partial \Phi_0} = -\frac{\Phi}{\Phi_0}\frac{\partial K_{dry}}{\partial \Phi}. \tag{B.26}$$

ξ with respect to $\mathbf{m_{HM}}$

$$\frac{d\xi}{dm_{HM}} = \frac{\partial \xi}{\partial K_{HM}}\frac{dK_{HM}}{dm_{HM}} + \frac{\partial \xi}{\partial \mu_{HM}}\frac{d\mu_{HM}}{dm_{HM}}, \tag{B.27}$$

with

$$\frac{\partial \xi}{\partial K_{HM}} = \frac{\mu_{HM}}{6}\frac{10\mu_{HM}}{(K_{HM} + 2\mu_{HM})^2} \tag{B.28}$$

and

$$\frac{\partial \xi}{\partial \mu_{HM}} = \frac{\xi}{\mu_{HM}} - \frac{K_{HM}}{\mu_{HM}}\frac{\partial \xi}{\partial K_{HM}}. \tag{B.29}$$

$\mu_{\mathbf{dry}}$ with respect to $\mathbf{m_{dry}}$

$$\frac{d\mu_{dry}}{dm_{dry}} = \frac{\partial \mu_{dry}}{\partial m_{dry}} + \frac{\partial \mu_{dry}}{\partial \mu_{VR}}\frac{d\mu_{VR}}{dm_{VR}} + + \frac{\partial \mu_{dry}}{\partial \mu_{HM}}\frac{d\mu_{HM}}{dm_{HM}} + \frac{\partial \mu_{dry}}{\partial \xi}\frac{d\xi}{dm_{HM}}, \tag{B.30}$$

with

$$\frac{\partial \mu_{dry}}{\partial \mu_{VR}} = \left[\frac{\mu_{dry} + \xi}{\mu_{VR} + \xi}\right]^2 \left(1 - \Phi/\Phi_0\right), \tag{B.31}$$

$$\frac{\partial \mu_{dry}}{\partial \mu_{HM}} = \left[\frac{\mu_{dry} + \xi}{\mu_{HM} + \xi}\right]^2 \Phi/\Phi_0, \tag{B.32}$$

$$\frac{\partial \mu_{dry}}{\partial \xi} = \frac{\partial \mu_{dry}}{\partial \mu_{VR}} + \frac{\partial \mu_{dry}}{\partial \mu_{HM}} - 1, \tag{B.33}$$

$$\frac{\partial \mu_{dry}}{\partial \Phi} = (\mu_{dry} + \xi)^2 \left[\frac{1/\Phi_0}{\mu_{VR} + \xi} - \frac{1/\Phi_0}{\mu_{HM} + \xi}\right] \tag{B.34}$$

and

$$\frac{\partial \mu_{dry}}{\partial \Phi_0} = -\frac{\Phi}{\Phi_0}\frac{\partial \mu_{dry}}{\partial \Phi}. \tag{B.35}$$

Derivatives of Hashin-Shtrikman stiff-sand model

This formulation has the same format as the previous soft-sand model, but changing μ_{HM} to μ_{VR} in K_{dry} derivative expressions, and the same change plus K_{dry} to K_{VR} in ξ derivatives, including the respective changes in differentiation variables.

Derivatives of Gassmann model

$\mathbf{K_{sat}}$ with respect to $\mathbf{m_{dry}}$

$$\frac{dK_{sat}}{dm_{dry}} = \frac{\partial K_{sat}}{\partial m_{dry}} + \frac{\partial K_{sat}}{\partial K_{VR}}\frac{dK_{VR}}{dm_{VR}} + \frac{\partial K_{sat}}{\partial K_{dry}}\frac{dK_{dry}}{dm_{dry}}, \tag{B.36}$$

with

$$\frac{\partial K_{sat}}{\partial K_{VR}} = 1 + \left[\frac{K_{VR} - K_{sat}}{K_{VR} - K_{dry}}\right]^2 + \Phi\left[\frac{K_{sat} - K_{dry}}{K_{VR} - K_{dry}}\right]^2\left(2\frac{K_{VR}}{K_{fl}} - 1\right), \tag{B.37}$$

$$\frac{\partial K_{sat}}{\partial K_{dry}} = \left[\frac{K_{VR} - K_{sat}}{K_{VR} - K_{dry}}\right]^2 \tag{B.38}$$

and

$$\frac{\partial K_{sat}}{\partial \Phi} = -\left[\frac{K_{sat} - K_{dry}}{K_{VR} - K_{dry}}\right]^2 K_{VR}\left(\frac{K_{VR}}{K_{fl}} - 1\right). \tag{B.39}$$

$\mathbf{K_{sat}}$ with respect to $\mathbf{m_{fl}} = \{\mathbf{S_w}, \mathbf{K_w}, \mathbf{K_{hc}}\}$

$$\frac{dK_{sat}}{dm_{fl}} = \frac{\partial K_{sat}}{\partial K_{fl}}\frac{dK_{fl}}{dm_{fl}}, \tag{B.40}$$

with

$$\frac{\partial K_{sat}}{\partial K_{fl}} = \left[\frac{K_{sat} - K_{dry}}{K_{VR} - K_{dry}}\right]^2 \Phi\left(\frac{K_{VR}}{K_{fl}}\right)^2, \tag{B.41}$$

$$\frac{dK_{fl}}{dS_w} = K_{fl}^2(1/K_{hc} - 1/K_w), \tag{B.42}$$

$$\frac{dK_{fl}}{dK_w} = S_w\left(\frac{K_{fl}}{K_w}\right)^2 \tag{B.43}$$

and

$$\frac{dK_{fl}}{dK_{hc}} = (1-S_w)\left(\frac{K_{fl}}{K_{hc}}\right)^2. \tag{B.44}$$

Derivatives of ρ with respect to $\mathbf{m}_\rho = \{\mathbf{V_{sh}}, \mathbf{\Phi}, \mathbf{S_w}, \rho_{\mathbf{g,sh,w,hc}}\}$

$$\frac{d\rho}{dV_{sh}} = (1-\Phi)(\rho_{sh}-\rho_g), \tag{B.45}$$

$$\frac{d\rho}{d\Phi} = S_w\rho_w + (1-S_w)\rho_{hc} - (1-V_{sh})\rho_g - V_{sh}\rho_{sh}, \tag{B.46}$$

$$\frac{d\rho}{dS_w} = \Phi(\rho_w - \rho_{hc}), \tag{B.47}$$

$$\frac{d\rho}{d\rho_g} = (1-\Phi)(1-V_{sh}), \tag{B.48}$$

$$\frac{d\rho}{d\rho_{sh}} = (1-\Phi)V_{sh}, \tag{B.49}$$

$$\frac{d\rho}{d\rho_w} = \Phi S_w \tag{B.50}$$

and

$$\frac{d\rho}{d\rho_{hc}} = \Phi(1-S_w). \tag{B.51}$$

Derivatives of velocities $\mathbf{v} = \{\mathbf{v_p}, \mathbf{v_s}\}$ with respect to $\mathbf{m} = \{\mathbf{\Phi}, \mathbf{S_w}, \mathbf{V_{sh}}, \mathbf{P}, \rho_{\mathbf{g,sh,w,hc}}, \mathbf{K_{g,sh,w,hc}}, \mu_{\mathbf{g,sh}}, \mathbf{C}, \mathbf{\Phi_0}\}$

$$\frac{dv}{dm} = \frac{\partial v}{\partial \rho}\frac{d\rho}{dm_\rho} + \frac{\partial v}{\partial K_{sat}}\frac{dK_{sat}}{dm_{dry,fl}} + \frac{\partial v}{\partial \mu_{dry}}\frac{d\mu_{dry}}{dm_{dry}}, \tag{B.52}$$

with

$$\frac{\partial v}{\partial \rho} = -\frac{v}{2\rho}, \tag{B.53}$$

$$\frac{\partial v_p}{\partial K_{sat}} = \frac{1}{2 v_p \rho}, \tag{B.54}$$

$$\frac{\partial v_p}{\partial \mu_{dry}} = \frac{4}{3}\frac{\partial v_p}{\partial K_{sat}} \tag{B.55}$$

and

$$\frac{\partial v_s}{\partial \mu_{dry}} = \frac{1}{2 v_s \rho}. \tag{B.56}$$

Bibliography

1 GRANA, D. et al. Stochastic inversion of facies from seismic data based on sequential simulations and probability perturbation method. *Geophysics*, v. 77, p. M53–M72, 2012. Cited on page 25.

2 BOSCH, M.; MUKERJI, T.; GONZALEZ, E. F. Seismic inversion for reservoir properties combining statistical rock physics and geostatistics: A review. *Geophysics*, v. 75, p. A165–A176, 2010. Cited 2 times on pages 25 and 26.

3 GRANA, D. et al. Probabilistic inversion of seismic data for reservoir petrophysical characterization: Review and examples. *Geophysics*, v. 87, p. M199–M216, 2022. Cited on page 25.

4 BULAND, A.; OMRE, H. Bayesian wavelet estimation from seismic and well data. *Geophysics*, Soc. of Expl. Geophys., v. 68, p. 2000–2009, 2003. Cited 4 times on pages 25, 27, 29, and 44.

5 GRANA, D.; ROSSA, E. D. Probabilistic petrophysical-properties estimation integrating statistical rock physics with seismic inversion. *Geophysics*, Soc. of Expl. Geophys., v. 75, p. O21–O37, 2010. Cited 3 times on pages 25, 26, and 27.

6 FIGUEIREDO, L. P. de; GRANA, D.; RODRIGUES, B. B. Gaussian Mixture Markov chain Monte Carlo method for linear seismic inversion. *Geophysics*, Soc. of Expl. Geophys., v. 84, p. R463–R476, 2019. Cited 7 times on pages 25, 26, 27, 29, 43, 48, and 49.

7 PENDREL, J.; SCHOUTEN, H. Facies — the drivers for modern inversions. *The Leading Edge*, v. 39, n. 2, p. 102–109, 2020. Cited 2 times on pages 25 and 26.

8 MAVKO, G.; MUKERJI, T.; DVORKIN, J. *The Rock Physics Handbook*. [S.l.]: Cambridge University Press, 2009. Cited 6 times on pages 25, 26, 29, 32, 78, and 79.

9 BULAND, A. et al. Bayesian lithology and fluid prediction from seismic prestack data. *Geophysics*, Soc. of Expl. Geophys., v. 73, p. C13–C21, 2008. Cited on page 25.

10 ZERILLI, A. et al. Realizing 4D CSEM value on deep water reservoirs – the Jubarte case study. In: *80th EAGE Conference & Exhibition 2018*. [S.l.]: EAGE, 2018. Cited 6 times on pages 25, 26, 27, 53, 65, and 67.

11 BUONORA, M. P. et al. mCSEM data interpretation for hydrocarbon exploration: A fast interpretation workflow for drilling decision. *Interpretation*, Soc. of Expl. Geophys., v. 2, p. HS1–HS11, 2014. Cited 2 times on pages 25 and 31.

12 MENEZES, P. T. et al. Time-lapse CSEM monitoring: Correlating the anomalous transverse resistance with SoPhiH maps. *Energies*, v. 14, p. 7159, 2021. Cited 3 times on pages 25, 63, and 65.

13 ALVAREZ, P. et al. Multiphysics characterization of reservoir prospects in the hoop area of the barents sea. *Interpretation*, v. 6, p. SG1–SG17, 2018. Cited 3 times on pages 25, 36, and 63.

14 MIOTTI, F. et al. A new petrophysical joint inversion workflow: Advancing on reservoir's characterization challenges. *Interpretation*, v. 6, p. SG33–SG39, 2018. Cited 3 times on pages 25, 49, and 63.

15 CONSTABLE, S. Ten years of marine CSEM for hydrocarbon exploration. *Geophysics*, v. 75, p. A67–A81, 2010. Cited on page 25.

16 ANDRéIS, D. et al. Overcoming scale incompatibility in petrophysical joint inversion of surface seismic and CSEM data. *SEG Technical Program Expanded Abstracts 2018*, Soc. of Expl. Geophys., n. 88, p. 2327–2331, 2018. Cited on page 25.

17 ZHDHANOV, M.; GRIBENKO, A.; WILSON, G. Generalized joint inversion of multimodal geophysical data using Gramian constraints. *Geophysical Research Letter*, v. 39, p. L09301, 2012. Cited on page 25.

18 HU, W.; ABUBAKAR, A.; HABASHY, T. M. Joint electromagnetic and seismic inversion using structural constraints. *Geophysics*, v. 74, p. R99–R109, 2009. Cited on page 26.

19 GAO, G.; ABUBAKAR, A.; HABASHY, T. M. Joint petrophysical inversion of electromagnetic and full-waveform seismic data. *Geophysics*, Soc. of Expl. Geophys., v. 77, p. WA3–WA18, 2012. Cited 2 times on pages 26 and 67.

20 HOVERSTEN, G. M. et al. Direct reservoir parameter estimation using joint inversion of marine seismic AVA and CSEM data. *Geophysics*, v. 71, p. C1–C13, 2006. Cited 2 times on pages 26 and 29.

21 CHEN, J. et al. A bayesian model for gas saturation estimation using marine seismic ava and csem data. *Geophysics*, v. 72, p. WA85–WA95, 2007. Cited on page 26.

22 TU, X.; ZHDANOV, M. S. Joint focusing inversion of marine controlled-source electromagnetic and full tensor gravity gradiometry data. *Geophysics*, v. 87, p. K35–K47, 2022. Cited on page 26.

23 CHEN, J.; HOVERSTEN, G. M. Joint inversion of marine seismic AVA and CSEM data using statistical rock-physics models and Markov random fields. *Geophysics*, v. 77, p. R65–R80, 2012. Cited 4 times on pages 26, 27, 31, and 49.

24 FIGUEIREDO, L. P. de et al. Multimodal Markov chain Monte Carlo method for nonlinear petrophysical seismic inversion. *Geophysics*, Soc. of Expl. Geophys., v. 84, p. M1–M13, 2019. Cited 2 times on pages 26 and 48.

25 AVDEEV, D. B. Three-dimensional electromagnetic modeling and inversion from theory to application. *Survey in Geophysics*, Springer, v. 26, p. 767–799, 2005. Cited on page 26.

26 FAGIN, S. W. 2. Seismic Modeling Approaches. In: *Seismic Modeling of Geologic Structures*. Society of Exploration Geophysicists, 1991. p. 9–44. Disponível em: <https://doi.org/10.1190%2F1.9781560802754.ch2>. Cited on page 26.

27 VALENTE, A. R.; NASCIMENTO, D.; COSTA, J. C. CSEM inversion using the correspondence principle: the adjoint-state approach. In: *Sixteenth International Congress of the Brazilian Geophysical Society*. [S.l.]: SBGF, 2021. Cited on page 26.

28 GRANA, D.; FJELDSTAD, T.; OMRE, T. Bayesian Gaussian Mixture linear inversion for geophysical inverse problems. *Mathematical Geosciences*, v. 49, p. 493–515, 2017. Cited 3 times on pages 26, 43, and 49.

29 ZOEPPRITZ, K. Viib. on reflection and transmission of seismic waves by surfaces of discontinuity. *Nachrichten von der Königlichen Gesellschaft der Wissenschaften zu Göttingen, Mathematisch-physikalische Klasse*, p. 66–84, 1919. Cited on page 26.

30 CREPALDI, J. L.; BUONORA, M. P.; FIGUEIREDO, I. Fast marine CSEM inversion in the CMP domain using analytical derivatives. *Geophysics*, Soc. of Expl. Geophys., v. 76, p. F303–F305, 2011. Cited 5 times on pages 26, 30, 32, 60, and 65.

31 BOSCH, M. The optimization approach to lithological tomography: Combining seismic data and petrophysics for porosity prediction. *Geophysics*, Soc. of Expl. Geophys., v. 69, n. 5, p. 1272–1282, 2004. Cited on page 26.

32 FIGUEIREDO, L. P. de et al. Bayesian seismic inversion based on rock-physics prior modeling for the joint estimation of acoustic impedance, porosity and lithofacies. *Journal of Computational Physics*, v. 336, p. 128–142, 2017. ISSN 0021-9991. Cited 3 times on pages 26, 27, and 34.

33 METROPOLIS, N. et al. Equations of state calculations by fast computing machines. *Journal of Chemical Physics*, Soc. of Expl. Geophys., n. 21, p. 1087–1092, 1953. Cited 3 times on pages 26, 43, and 49.

34 TARANTOLA, A. *Inverse Problem Theory.* [S.l.]: Siam, 2005. Cited 6 times on pages 27, 35, 43, 49, 57, and 65.

35 PUJOL, J. The solution of nonlinear inverse problems and the Levemberg-Marquardt method. *Geophysics*, v. 72, p. W1–W16, 2007. Cited 2 times on pages 27 and 49.

36 SARAIVA, M. et al. *Data-driven Full-waveform Inversion Surrogate using Conditional Generative Adversarial Networks.* 2021. Cited on page 29.

37 AKI, K.; RICHARDS, P. *Quantitative seismology.* [S.l.]: University Science Books, 2002. Cited 2 times on pages 29 and 60.

38 CASTAGNA, J. P.; BACKUS, M. M. *Offset-Dependent Reflectivity-Theory and Practice of AVO Analysis.* [S.l.]: Society of Exploration Geophysicists, 1993. Cited on page 29.

39 LONGMAN, I. M. The calculation of ricker seismic wavelet functions. *Geophysics*, v. 45, n. 6, p. 1055–1060, 1980. Cited on page 29.

40 UM, E. S.; ALUMBAUGH, D. L. On the physics of the marine controlled-source electromagnetic method. *Geophysics*, Soc. of Expl. Geophys., v. 72, p. WA13–WA26, 2007. Cited 2 times on pages 30 and 36.

41 CONSTABLE, S.; SRNKA, L. J. Special section — marine controlled-source electromagnetic methods: An introduction to marine controlled-source electromagnetic. *Geophysics*, Soc. of Expl. Geophys., v. 72, p. WA3–WA12, 2007. Cited on page 30.

42 KEY, K. 1D inversion of multicomponent, multifrequency marine CSEM data: Methodology and synthetic studies for resolving thin resistive layers. *Geophysics*, Soc. of Expl. Geophys., v. 74, n. 2, p. 9–20, 2009. Cited on page 32.

43 MITTET, R. et al. CMP inversion and post-inversion modelling for marine CSEM data. *first break*, Europ. Assoc. of Geosc. Eng., v. 26, p. 59–67, 2008. Cited on page 32.

44 GRANA, D. Bayesian linearized rock-physics inversion. *Geophysics*, v. 81, n. 6, p. D625–D641, 2016. Cited 2 times on pages 34 and 43.

45 TALARICO, E. C. S. et al. Multiple response nonlinear regression applied to simultaneous density, vp and vs rock physics calibration and related statistical analysis. In: *15th International Congress of the Brazilian Geophysical Society*. [S.l.]: Brazilian Geophysical Society, 2017. Cited on page 34.

46 SIMANDOUX, P. Dielectric measurements in porous media and application to shaly formation. *Revue de L'Institut Français du Pétrole*, L'Institut Français du Pétrole., n. 18, p. 193–215, 1963. Cited on page 34.

47 GLOVER, P. W. J. A generalized Archie's law for n phases. *Geophysics*, Soc. of Expl. Geophys., v. 75, p. E247–E265, 2010. Cited 2 times on pages 34 and 80.

48 BROMILEY, P. Products and convolutions of Gaussian probability density functions. *Tina-Vision Memo*, v. 3, p. 1, 2003. Cited on page 45.

49 PETERSEN, K. B.; PETERSEN, M. S. *The matrix cookbook*. [S.l.]: Technical University of Denmark, 2012. Cited on page 45.

50 TALARICO, E. C. S. et al. Uncertainty quantification in seismic facies inversion. *Geophysics*, v. 85, p. M43–M56, 2020. Cited on page 48.

51 MARQUARDT, D. W. An algorithm for least-squares estimation of nonlinear parameters. *Journal of the Society for Industrial and Applied Mathmatics*, v. 11, p. 431–441, 1963. Cited on page 49.

52 FRISCH, K. The logarithmic potential method of convex programming. *Memorandum, University Institute of Economics, Oslo*, v. 5, n. 6, 1955. Cited on page 51.

53 SANTOS, W. G.; RéGIS, C. R. A study of the electromagnetic field from the MCSEM diploe source in an anisotropic layered earth. *Brazillian Journal of Geophysics*, Braziliian Soc. of Geophys., v. 33, p. 277–294, 2015. Cited on page 53.

54 NEWMAN, G. A.; COMMER, M.; CARAZZONE, J. J. Imaging CSEM data in the presence of electrical anisotropy. *Geophysics*, Soc. of Expl. Geophys., v. 75, p. F51–F61, 2010. Cited on page 53.

55 ABUBAKAR, A. et al. A 3D parametric inversion algorithm for triaxial induction data. *Geophysics*, v. 71, p. G1–G9, 2006. Cited on page 53.

56 NABIGHIAN, M. N. *Electromagnetic Methods in Applied Geophysics Theory*. [S.l.]: Society of Exploration Geophysics, 1987. v. 1. Cited on page 65.

57 BATZLE, M. L.; WANG, Z. Seismic properties of pore fluids: Geophysics. *Geophysics*, Soc. of Expl. Geophys., v. 57, p. 1396–1408, 1992. Cited on page 80.